

# Artificial-intelligence-driven discovery of catalyst *genes* with application to CO<sub>2</sub> activation on semiconductor oxides

A. Mazheika<sup>1,\*</sup>, Y. Wang<sup>1,2</sup>, R. Valero<sup>3,4</sup>, F. Viñes<sup>3</sup>, F. Illas<sup>3</sup>, L. M. Ghiringhelli<sup>1,5</sup>, S. V. Levchenko<sup>6,\*</sup>, M. Scheffler<sup>1,5</sup>

<sup>1</sup>The NOMAD Laboratory at the Fritz-Haber-Institut der Max-Planck-Gesellschaft, 14195 Berlin-Dahlem, Germany

<sup>2</sup>Department of Chemistry and Guangdong Provincial Key Laboratory of Catalysis, Southern University of Science and Technology, Shenzhen 518055, Guangdong, China

<sup>3</sup>Departament de Ciència de Materials i Química Física and Institut de Química Teòrica i Computacional (IQTCUB),

Universitat de Barcelona, c/ Martí i Franquès 1, Barcelona 08028, Spain

<sup>4</sup>Zhejiang Huayou Cobalt Co.,Ltd., No. 18 Wuzhen East Road, Tongxiang Economic Development Zone, Jiaxing, Zhejiang 314500, China

<sup>5</sup>The NOMAD Laboratory at the Humboldt University of Berlin, 12489 Berlin, Germany

<sup>6</sup>Skolkovo Institute of Science and Technology, Skolkovo Innovation Center, Bolshoy Boulevard 30, bld. 1, 121205 Moscow, Russia

\*corresponding authors: [alex.mazheika@gmail.com](mailto:alex.mazheika@gmail.com); [s.levchenko@skoltech.ru](mailto:s.levchenko@skoltech.ru)

## Abstract

Catalytic-materials design requires predictive modeling of the interaction between catalyst and reactants. This is challenging due to the complexity and diversity of structure-property relationships across the chemical space. Here, we report a strategy for a rational design of catalytic materials using the artificial intelligence approach (AI) subgroup discovery. We identify catalyst *genes* (features) that correlate with mechanisms that trigger, facilitate, or hinder the activation of carbon dioxide (CO<sub>2</sub>) towards a chemical conversion. The AI model is trained on first-principles data for a broad family of oxides. We demonstrate that

surfaces of experimentally identified good catalysts consistently exhibit combinations of *genes* resulting in a strong elongation of a C-O bond. The same combinations of *genes* also minimize the OCO-angle, the previously proposed indicator of activation, albeit under the constraint that the Sabatier principle is satisfied. Based on these findings, we propose a set of new promising catalyst materials for CO<sub>2</sub> conversion.

## Introduction

The need for converting stable molecules such as carbon dioxide (CO<sub>2</sub>), methane, or water into useful chemicals and fuels is growing quickly along with the depletion of fossil-fuel reserves and the pollution of the environment<sup>1-3</sup>. Such a conversion does not have a satisfactory solution, so far. In particular, CO<sub>2</sub> conversion remains one of the most important societal and technological challenges<sup>1,2,4-8</sup>.

The general understanding in heterogeneous catalysis is that a stable molecule such as CO<sub>2</sub> needs to be “prepared”, before its catalytic conversion occurs. This leads to the notion of molecular activation<sup>9</sup>. However, on one hand, this notion encompasses a very wide variety of processes (adsorption, photo-excitation, application of electric field, etc.) and materials (including compositional and structural variability), and it remains unclear which properties of the catalytic material and the adsorbed molecule determine the final chemistry, what is the relationship between the two sets of properties, and how general this relationship may be. On the other hand, finding the set of descriptive parameters of a catalytic material that characterize the catalytic performance in a particular process, or even in general for a given reactant, would be very valuable, because it would allow us to quickly search for promising candidate catalysts using rational design<sup>10-17</sup>. We call these properties materials *genes*. The *genes* do not necessarily correlate with catalytic activity by themselves. Similarly to biological genes, their role depends on the combination in which they occur, and can be either beneficial or detrimental to the catalytic activity.

Several strategies exist to find such properties for a given reaction. One way is to explore the free-energy surface for each catalyst candidate, which is a slow and resource-consuming process, and currently computationally unfeasible for many materials on a high-throughput basis. An alternative approach consists in searching for a correlation between experimentally determined material's properties and its catalytic performance. Such a strategy requires consistent experimental measurements at well-defined conditions for a set of materials. To the best of our knowledge, such consistent data have not been reported so far for CO<sub>2</sub> conversion on semiconductor oxides. Moreover, available publications usually

do not report unsuccessful experimental results. These issues and a strategy to address them have been recently discussed in our publication<sup>18</sup>.

Yet another strategy is to find an indicator of activation, namely, a property of the system that directly indicates certain catalytic performance of the material<sup>10</sup>. Indicators are distinguished from materials *genes* based on a qualitatively different level of computational complexity. The indicator can still be unfeasible or hard for a high-throughput study of hundreds of thousands or millions of materials. However, when it can be calculated for a few tens or hundreds of materials in a reasonable time, these data can then be used to find materials *genes* that control the value of the indicator. Since a direct search for a relationship between the indicator and catalytic performance of a material would also require a consistent set of data of turnover frequency (TOF), selectivity, and yield values, one could instead consider several most promising indicators, find out which materials are good catalysts, and then check which indicators correlate with this observation. This approach also addresses the problem of defining activation in terms of the adsorbed-molecule properties as potential indicators of catalytic activity.

Catalytic conversion of CO<sub>2</sub> requires activation of other reactants as well, e.g. molecular hydrogen, water, or methane. In particular hydrogen can serve as an environmentally friendly reagent that can be produced by water electrolysis or photo-splitting avoiding extra CO<sub>2</sub> emissions.<sup>19-21</sup> Also, oxygen vacancies have been proposed as active sites for CO<sub>2</sub> conversion on some materials.<sup>22</sup> Therefore, predictions of catalytic activity of materials for CO<sub>2</sub> conversion can be refined based on analysis of activation of other reactants and defects. An additional challenge is to ensure that the useful products as well as the surface catalytic activity are preserved under the conditions of activation and subsequent conversion. While the strong C-O double bonds in CO<sub>2</sub> can be weakened or even broken by adsorption at a solid surface at an elevated temperature, this may also lead to a too strong adsorption or further dissociation of the molecule, so that the catalytic surface is poisoned by carbonate or carbon deposits. A weak adsorption, on the other hand, means no activation.

In this work, we combine first-principles calculations with an artificial-

intelligence (AI) method, subgroup discovery (SGD), to identify pristine materials properties that optimize indicators of catalytic CO<sub>2</sub> activation. Moreover, SGD allows identifying one or more distinct combinations of materials features (*genes*) that promote activation. We focus on oxide materials as candidate catalysts. Oxides are structurally and compositionally stable under realistic temperatures and can be less expensive than the traditional precious metal-containing catalysts<sup>23-25</sup>. Activation of other reactants and defects are not considered. As shown below, meaningful predictions can be made based solely on the analysis of adsorption properties of CO<sub>2</sub> on pristine surface. This confirms that these properties are good indicators of activation with a viable optimization pathway at least for the chosen class of materials. The Sabatier principle is taken into account by ensuring that the adsorption energy is not too large or too small. In order to ensure reproducibility of our AI data analysis, we provide all necessary metadata (input parameters) and workflow in the easily accessible form of a Jupyter notebook<sup>26</sup>. We argue that, with the ever-growing importance and complexity of AI, such detailed and tutorial documentation is a necessity of good scientific practice. Our approach is applicable to a wider class of materials and molecules, not limited to oxides or CO<sub>2</sub>. Our study by no means encompasses all possible mechanisms of CO<sub>2</sub> conversion on oxide surfaces, but it offers a clear design path among many possible ones.

## Results

**CO<sub>2</sub> activation.** We find that on semiconductor oxide surfaces CO<sub>2</sub> is chemisorbed exclusively when the carbon atom binds to surface O-atoms. All other minima of the potential-energy surface are found to be either metastable or correspond to physisorption. Therefore, there are as many different potential chemisorption sites as there are unique O atoms at the surface. The data set includes all non-equivalent surface O atoms on the 141 considered surfaces of 71 materials, which sum up to 255 unique adsorption sites. Among these sites on about 4% (10 out of 255) CO<sub>2</sub> prefers to physisorb, *i.e.* any chemisorbed state is metastable with respect to the physisorbed one. The physisorption can be easily identified by an almost linear geometry of the adsorbed molecule, and a C-O bond

distance very close to the C-O bond length in a gas-phase CO<sub>2</sub> molecule, 1.17 Å.

We considered six different candidate indicators of CO<sub>2</sub> activation, including OCO-angle and C-O bond distance. Bending of the OCO angle in the adsorbed CO<sub>2</sub> molecule relative to the gas-phase value of 180° (linear configuration) has been previously proposed<sup>27</sup> and widely accepted as a good indicator of activation. For gas-phase CO<sub>2</sub>, it is understood that the C-O double bond is weakened when an electron is added to the lowest unoccupied orbital, because it is of antibonding ( $\pi^*$ ) character with a concomitant bending of the molecule. There is a one-to-one mapping between the C-O bond length  $l(\text{C-O})$  and the OCO angle in gas-phase CO<sub>2</sub><sup>δ-</sup> for a range of  $\delta > 0$  (red curve in Fig. 1). However, this is not the case for the adsorbed CO<sub>2</sub> (dots in Fig. 1). There is a subset of adsorbed CO<sub>2</sub> that is close to the red line, but there are many cases where  $l(\text{C-O})$  is substantially larger for a given OCO angle. This is in contrast to metal alloy nanoparticle catalysts, where there is a better correlation between OCO angle and  $l(\text{C-O})$ <sup>28</sup>. Also, a longer C-O bond reflects a weakening and readiness for further chemical transformations. Thus, the bond elongation itself may be an alternative indicator of activation. A look at the adsorbed CO<sub>2</sub> structures reveals that, on sites following the gas-phase correlation, the molecule adsorbs in nearly symmetric adsorption structures with nearly equal length of the two C-O bonds. In the other cases one O atom of CO<sub>2</sub> is close to surface cation(s), leading to a pronounced asymmetry of the adsorbed molecule.

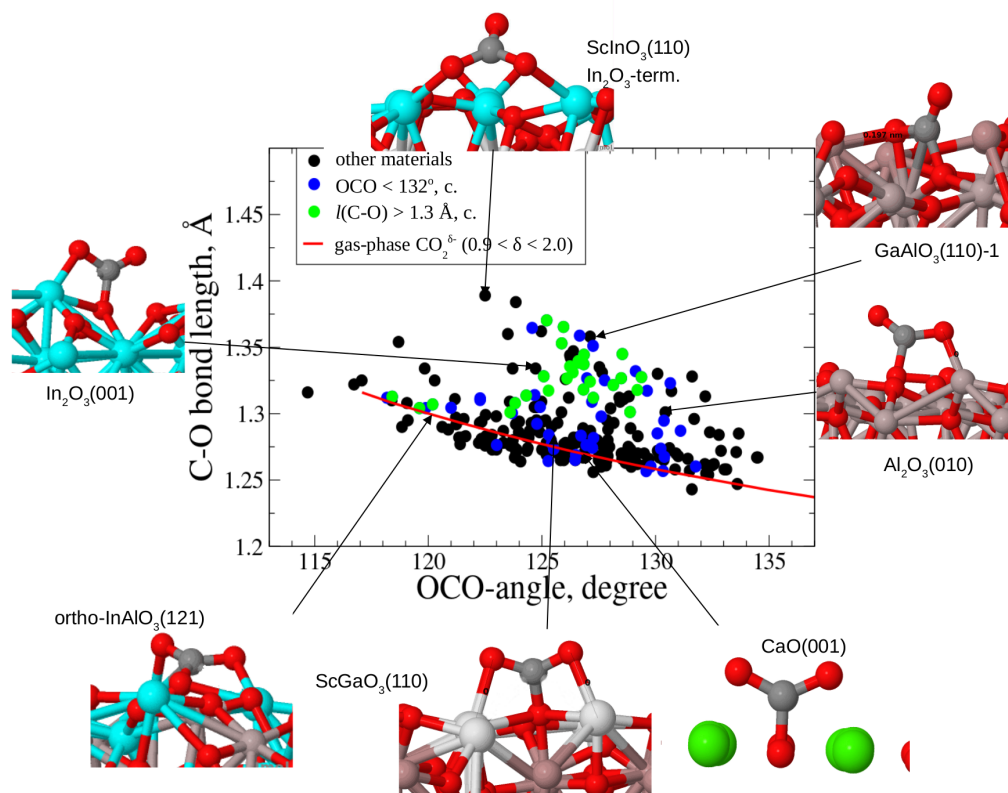


**Figure 1. Correlation between the larger of the two C-O bond lengths and the OCO-angle for charged gas-phase and adsorbed CO<sub>2</sub>.** The OCO-angle in charged gas-phase CO<sub>2</sub> is shown with the red line, and adsorbed CO<sub>2</sub> structures are shown with the dots. Colored dots: blue – adsorption sites from the unconstrained subgroup with OCO < 132°, green – subgroup of sites with  $l(\text{C-O}) > 1.30 \text{ \AA}$ , black – the remaining samples (see the text). The subgroups obtained with Sabatier principle constraint are marked with “c.”.

Other considered potential indicators of activation include Hirshfeld charge<sup>29</sup> of adsorbed CO<sub>2</sub> (a direct indicator of the charge transferred to CO<sub>2</sub>), dipole moment of the surface along the surface normal per adsorbed CO<sub>2</sub> molecule (includes charge transfer to the molecule, as well as adsorption induced surface relaxation), the difference in Hirshfeld charges of C and O atoms in an adsorbed CO<sub>2</sub> molecule (indicates the ionicity of C-O bonds), and the difference in Hirshfeld charges of the O atoms in the adsorbed molecule (indicates asymmetry of the adsorbed molecule).<sup>29,9</sup>

**Subgroup discovery.** To find out which properties (features) of the clean

surfaces determine when a given activation indicator is maximized or minimized, we employ the subgroup-discovery (SGD) approach<sup>30-34</sup>. Given a dataset and a target property known for all data points, the SGD algorithm identifies subgroups with “outstanding characteristics” (see further for the criteria for being outstanding) and describes them by means of conjunction of basic propositions (selectors) of the kind “( $f_1 < a$ ) AND ( $f_2 \geq b$ ) AND ...”, where  $f_i$  is a feature and  $a$ ,  $b$  are threshold values also found by SGD. In the framework of SGD, we call the selected primary features  $\{f_1, f_2, \dots\}$  materials *genes*. Thus, SGD identifies both the outstanding subgroups and the relevant materials *genes* for a given target property.

Obviously, the selectors should only contain features that are much easier to evaluate than the target property. In presented work, the considered features include properties of gas-phase atoms that build the material, and properties of the pristine material (properties of the bulk phase and of the pristine relaxed surface). Overall 46 primary features have been considered. The full list is presented Supplementary Table 3. Our strategy is to provide an almost exhaustive list of features, and use data analytics to select materials *genes* from this list. Some of these features have been explored previously as descriptors of catalytic activity for semiconducting and metallic oxides.<sup>35,36,37,38</sup> O 2p band center features have been shown to correlate with catalytic properties of both semiconducting and metallic oxides.<sup>35,37</sup> In particular, most of the features (or closely related ones) mentioned in Ref. 36, inspired by the work of Grasselli<sup>39</sup>, are included in our set, except oxygen vacancy formation energy, which is relevant for the oxidation catalysis, while here we are interested in partial or complete reduction. Additional important features in our work (see below) include features related to polarizability of surface cations, which describe long-range surface response to charged adsorbates. A subset of features from our list have been recently used successfully for predicting catalytic properties of metallic oxides<sup>38</sup>, along with additional features relevant specifically for metallic oxides (such as partial electronic state fillings).

The features selected by the SGD are summarized in Table 1.

The outstanding subgroup should satisfy several criteria. It should be

statistically relevant; therefore the subgroups of too small size should be penalized. Target property values (OCO-angle, C-O bond length, etc.) for subgroup samples should be as different as possible from corresponding gas-phase values since their change upon adsorption indicates CO<sub>2</sub> activation<sup>33</sup>. To achieve this, two requirements are imposed simultaneously: (i) The target-property values for subgroup members should be smaller or larger (depending on the target) than a certain value (a cutoff), and (ii) the target-property values are minimized or maximized within the cutoff. The latter condition gives preference to subgroups with smaller or larger target property values among similarly sized subgroups within the cutoff. The value of the cutoff is a parameter. As it approaches the optimal value of an activation indicator among all data points, additional or alternative materials *genes* and their combinations leading to stronger activation are identified. We explore the whole range of the parameter for each target property (for OCO-angle - 123°, 124°, 126°, 128°, 130°, and 132°; for *l*(C-O) - 1.26 Å, 1.28 Å, and 1.30 Å).

In addition to these criteria, we consider the requirement that adsorption energies are not too strong and not too weak for most of the samples in a subgroup. Strong activation (i.e., strong weakening of the C-O bonds) can be achieved by strong binding to the surface. It is well known that good catalytic performance requires a balanced adsorption strength. This is known as Sabatier principle. In addition to the practical value of identifying subgroups that satisfy this principle, comparison of subgroup selectors obtained with and without this requirement helps to identify combinations of materials features that promote desired changes in target properties and at the same time yield intermediate adsorption energies.

Sabatier principle is reflected by a characteristic volcano-type behavior of catalytic activity as a function of adsorption energy of reactants and intermediates. Position of the top of volcano depends on particular reaction and conditions. It can be estimated from condition  $|\Delta G| \sim 0$ , where  $\Delta G$  is the Gibbs free energy of adsorption. For CO<sub>2</sub> adsorption at room temperature and partial CO<sub>2</sub> pressure of 1 atm this condition corresponds to about -0.5 eV adsorption energy<sup>40</sup>. At temperatures around 450 °C (typical conditions for CO<sub>2</sub> methanation<sup>41</sup>)  $\Delta G = 0$

corresponds to adsorption energy  $-1.7 \text{ eV}^{41}$ . Therefore, for catalytic conversion at low or moderate temperatures this implies that  $\text{CO}_2$  adsorption energies should be in the range from between  $-2.0$  and  $-0.5 \text{ eV}$ .

These requirements are implemented in the following quality functions that are maximized during the search for subgroups. In particular, for OCO-angle minimization we use:

$$F(Z) = \theta_{\text{cut}} \left[ \frac{s(Z)}{s(Y)} \cdot \left( \frac{\max(Z) - \alpha_g}{\min(Y) - \alpha_g} \right) \cdot u(p) \right] \quad (1)$$

and for C-O bond maximization the following quality function was applied:

$$F(Z) = \theta_{\text{cut}} \left[ \frac{s(Z)}{s(Y)} \cdot \left( \frac{\min(Z) - l_g}{\max(Y) - l_g} \right) \cdot u(p) \right] \quad (2)$$

where  $Y$  is the whole data set,  $Z$  - a subgroup,  $s$  - size (number of data points),  $\min$  and  $\max$  - minimal or maximal value of the target property,  $\alpha_g$  and  $l_g$  are the gas-phase values of OCO-angle and C-O bond distance,  $180^\circ$  and  $1.17 \text{ \AA}$  respectively, and  $\theta_{\text{cut}}$  is the Heaviside step function which is equal 1 if all data points in the subgroup satisfy the cutoff condition and 0 otherwise. Thus, larger values of the quality function  $F(Z)$  are obtained for those subgroups in which minimal (maximal) value of a target property is close to the maximal (minimal) value of the whole sampling with respect to the gas-phase value of  $\text{CO}_2$  molecule. The use of maximum/minimum instead of a median is done to ensure that a target property is optimal for as many members of a subgroup as possible. The gas-phase reference values are usually significantly different from the "chemisorption" subset. Therefore, the term in squared brackets in eq. (1) and (2) can noticeably contribute only when sizes of candidate subgroups are similar.

The term  $u(p)$  in eq. (1) and (2) is added in order to account for Sabatier principle in SGD framework. We have implemented a multitask quality function, where a factor  $u(p)$  increases quality of subgroups with adsorption energies falling within this range. This is formulated in terms of the information gain<sup>34</sup>, *i.e.*, reduction of the normalized Shannon entropy. We perform the SGD for each target property both explicitly accounting for the Sabatier principle and without it. The latter case is equal to  $u(p) = 1$  in eq. (1) and (2).<sup>34</sup>

We note that SGD is qualitatively different from machine-learning classification/regression techniques such as neural networks, kernel regression methods, or decision-tree regression (DTR<sup>42</sup>) (e.g., random forest). SGD is typically referred to as a supervised descriptive rule-induction technique<sup>43</sup>, *i.e.*, it uses the labels assigned to the data points (the values of the target property) in order to identify patterns in the data distribution (the statistically exceptional data groups) and the rules defining them (the selectors), by optimizing a quality function which is a functional of the distribution of values of the target property<sup>43</sup>. While there are apparent similarities between SGD and DTR as both methods yield models in terms of physically interpretable selectors (usually, inequalities) on a selected subset of the input features, the analogy stops at this level, as SGD focuses at (and only at) subgroups from the very beginning and says nothing about the data that are not in the subgroup. In contrast, DTR determines a global partitioning of the input space by minimizing a global quality function, *i.e.*, the quality of a single subset is secondary with respect to the resulting quality of all subsets partitioning the whole data set. In other words, for finding distinct combinations of materials *genes* driving desirable changes in a particular target property (possibly different combinations leading to the same result), the SGD approach has a significantly higher flexibility and reliability. This is demonstrated below for a DTR analysis for our target properties.

The metadata and workflow for the AI analysis is documented in the Jupyter notebook<sup>26</sup>.

**Results of the subgroup discovery.** The SGD for OCO angles was done with eq. (1) for the quality function, and OCO as a target property, since smaller angles indicate larger charge transferred to the molecular  $\pi^*$  orbital. The subgroup selectors obtained with different OCO angle cutoffs (126°, 128°, 130°, and 132°) with or without the adsorption energy constraint are listed in Table 2 (for more details see the Supplementary Table 4). Analysis of these subgroups reveals that the angle reduction is determined by an interplay of several factors: an electron transfer from the cations to surface O atoms, delocalization of electron density between cations and O atoms, and coordination of the surface O atoms. Without the Sabatier principle constraint, the OCO angle reduction below 132° is mainly

due to the electron accumulation at the O atom of the clean surface. This is expressed by the conditions of more negative Hirshfeld charge on O-atoms ( $q_o < \dots$ ), not very low IP of at least one cation ( $IP_{\max} > \dots$ ), and increased polarizability of the surface O atom on which  $\text{CO}_2$  is adsorbed ( $C_6^o > \dots$ ). Upon adsorption of  $\text{CO}_2$ , this charge on the surface O-atom is readily available for transfer to  $\text{CO}_2$ . When the Sabatier principle constraint is introduced, the  $\text{OCO} < 132^\circ$  subgroup also includes sites with a pronounced electron transfer to  $\text{CO}_2$ , but with a lower-energy O 2p band maximum ( $M < \dots$ ) with respect to vacuum level, and a larger kurtosis ( $kurt > \dots$ ). These conditions imply reduced inter-electronic repulsion around the surface O atom achieved by partial delocalization of the charge density.

At lower OCO cutoffs, the subgroup selectors include coordination descriptors  $Q_i$ ,  $i = 5, 6$ . Without Sabatier principle, sites with larger  $Q_i$  are selected, and *vice versa*. Larger  $Q_i$  indicate lower coordination of the O atom. This reduces electron repulsion and therefore facilitates electron transfer to the O atom of the clean surface. However, this also increases the bonding strength of  $\text{CO}_2$  to the surface. This explains why selectors of subgroups obtained with Sabatier principle include the opposite conditions ( $Q_5 < \dots$ ).

Other surface features describing electron distribution are related to Madelung potential: electrostatic potential and field ( $\varphi_{1.4}$ ,  $\varphi_{2.6}$ , and  $\Delta\varphi = \varphi_{1.4} - \varphi_{2.6}$ ) and distances between the O atom and surface cations. More open surface structure with larger distances between cations at the O site facilitates charge transfer to adsorbed  $\text{CO}_2$  molecule, since the Madelung potential from the nearby cations is reduced. This is reflected in appearance of propositions involving features  $d_1$ ,  $d_2$ , and  $d_3$ . For example, for the  $\text{OCO} \leq 130^\circ$  subgroups, imposing energy constraint changes proposition ( $d_1 > \dots$ ) to ( $d_1 < \dots$ ), which implies an increased energy cost for transferring electrons to  $\text{CO}_2$ . Larger electric fields  $\Delta\varphi$  around the adsorption site imply stronger localization of electron density on O atoms, and thus also improve efficiency of charge transfer to the adsorbed molecule.

The smaller OCO subgroups with Sabatier principle also include propositions implying increased polarizability of both cations ( $C_6^{\min} > \dots$ ). Another support-

defining condition is that the radius of the lowest unoccupied orbital for the metal atoms should not be small ( $r_{+1} \geq \dots$ ). This requirement is true for most cations with negative electron affinities (Supplementary Figure 4). Analysis of adsorbed CO<sub>2</sub> structures and Hirshfeld charges reveals that this condition together with the higher polarizability of cations at the *pristine* surface encompass two scenarios: (i) additional electron transfer to CO<sub>2</sub> upon adsorption and (ii) stronger binding between O atoms in CO<sub>2</sub> and surface cations. When scenario (ii) dominates, CO<sub>3</sub><sup>δ-</sup> anion lies nearly horizontally at the surface, and is bound with nearby cations by chemical bonds via its oxygen atoms. Such a structure leads to small OCO angles in CO<sub>3</sub><sup>δ-</sup> (around 120°), even if charge transfer is limited. Thus, increased bending of adsorbed CO<sub>2</sub> occurs due to charge transfer over larger distances and/or distortion of the adsorbed molecule and the surface, both leading to a weaker adsorption. The cases where both scenarios are active include the same sites as in the subgroups with elongated  $l(\text{C-O})$ , as described below.

In order to obtain the subgroups of adsorption sites with larger  $l(\text{C-O})$ , we performed the SGD with the quality function eq. (2) and  $l(\text{C-O})$  as target property. The results for  $l(\text{C-O})$  cutoffs 1.26, 1.28, and 1.30 Å are summarized in Table 2 and Supplementary Table 5. In contrast to OCO, the analysis of the obtained top subgroups shows a much less pronounced or no effect of imposing Sabatier principle on the distribution of adsorption energies within the subgroups. This is because sites with too strong adsorption are excluded based on  $l(\text{C-O})$  threshold alone, without the need to introduce the energy constraint. For example, the range of  $l(\text{C-O})$  for the top  $l(\text{C-O}) > 1.26$  Å subgroup without constraining adsorption energies is the same as for the top OCO < 130° subgroup, but it contains significantly more sites with intermediate adsorption energies.

Electron transfer to an adsorbed CO<sub>2</sub> molecule increases both the OCO bending and C-O bond elongation. The main difference between OCO and  $l(\text{C-O})$  subgroups is that in the latter an additional mechanism of increasing  $l(\text{C-O})$  is in effect, namely a covalent bonding between one O atom of the CO<sub>2</sub> molecule and the nearest surface cation. This can be concluded from the analysis of adsorption geometries, and correlates with the presence of proposition ( $EA_{\text{max}} \leq 0.005$  eV), selecting cation species that can accept electron density, e.g. from an O atom in

adsorbed CO<sub>2</sub> molecule. Other proposition that appears in most selectors of top subgroups is ( $d_2 > 2.14 \text{ \AA}$ ) or ( $d_2 > 2.22 \text{ \AA}$ ) - larger distances to the second nearest cation from an O-atom. Larger elongation of the C-O bond is achieved by asymmetry of the cation types at the surface, where one can bind an O atom of the adsorbed CO<sub>2</sub>, while the other (located further away) cannot. An example asymmetric CO<sub>2</sub> adsorption structure is shown in Supplementary Figure 5.

Other propositions indicate a moderate charge transfer to adsorbed CO<sub>2</sub> molecule as in the case of OCO subgroups with adsorption energy constraint. Propositions ( $M \geq -8.05 \text{ eV}$ ), ( $PC \geq -9.32 \text{ eV}$ ) in  $l(\text{C-O}) < 1.26 \text{ \AA}$  subgroups imply enhanced charge density on the surface O-atoms, since electron-electron repulsion raises energies of O 2p band states. However, at larger  $l(\text{C-O})$  cutoffs the electron transfer is balanced by such propositions as ( $M \leq -5.19 \text{ eV}$ ), ( $U \leq -4.92 \text{ eV}$ ), and ( $W \geq 5.10 \text{ eV}$ ) indicating limited electron transfer. These propositions point to a more covalent bonding between cations and surface O atom. Rather persistent proposition observed in many selectors of  $l(\text{C-O})$  subgroups is the limit of minimal charge on surface cations ( $q_{\min} < 0.48e$ ). It also shows the limitation of the charge transfer from one type of cations to surface oxygen atoms.

In general, we find that subgroups obtained with smaller cutoffs do not have a strong overlap with subgroups with larger cutoffs for OCO. In particular, for subgroups with close cutoffs the overlap can be smaller than 50% of the smaller subgroup (but is never below 30%). Interestingly, for  $l(\text{C-O})$  the situation is opposite: subgroups with tighter cutoffs are mostly contained in the subgroups for more relaxed constraints. This means that, while larger values of  $l(\text{C-O})$  are mainly controlled by the same or additional *genes*, smaller values of OCO are due to alternative *genes*. The overlap of OCO subgroups becomes even smaller when Sabatier principle is included, confirming the absence of a universal mechanism for OCO angle reduction that is compatible with moderate adsorption energy.

In summary, we find that, while an increased electron density at the O adsorption site is necessary for chemisorption and leads to both OCO bending and C-O bond elongation in an adsorbed CO<sub>2</sub> molecule, there are additional actuators for these effects that are different for different target properties. The OCO angle is

in general minimized by increasing electron transfer to the O site. However, this also leads to a strong adsorption for many materials (Figure 2). To satisfy Sabatier principle, the electron transfer to CO<sub>2</sub> must be moderate. This is achieved by delocalization of charge density around O sites and/or by distortion of the adsorbed molecule due to formation of covalent bonds between O atoms in CO<sub>2</sub> and surface cations. The largest C-O bond elongations are achieved when both charge transfer to adsorbed CO<sub>2</sub> and the covalent interaction are present, and local geometry around surface O-atom provides the asymmetry in adsorption structure. This mechanism automatically fulfills the Sabatier principle.

The subgroups found by SGD for the dipole moment induced by CO<sub>2</sub> adsorption, its total Hirshfeld charge, and the difference of charges on C and O atoms significantly overlap with the subgroup of smaller OCO-angles. The subgroup found by maximizing the difference of Hirshfeld charges on O-atoms of an adsorbed CO<sub>2</sub> largely overlaps with the subgroup of sites delivering larger  $l(\text{C-O})$ . In general, these indicators are not better than OCO or  $l(\text{C-O})$ . Therefore, below we focus on OCO angle and  $l(\text{C-O})$  as indicators of CO<sub>2</sub> activation. More details about the other indicators can be found in Supplementary discussion.

**Comparison with experimental results.** To address the question which of the discussed properties can serve as indicator of the catalytic activity, we compare our predictions to reported experimental results (Table 3). It should be stressed that the available experimental data are scarce, and results are difficult to compare quantitatively. We consider thermally- and, for completeness, some photo-driven catalysis and thus also include supported metal catalysts with the considered oxides as support. Despite possibly different mechanisms for CO<sub>2</sub> conversion in the different types of catalysis, we believe that the properties of adsorbed CO<sub>2</sub> molecule can still serve as indicators of the catalytic activity. Thus, it is possible that under such daunting situation a reliable indicator of CO<sub>2</sub> activation can still be identified. As described below, our analysis confirms this hope.

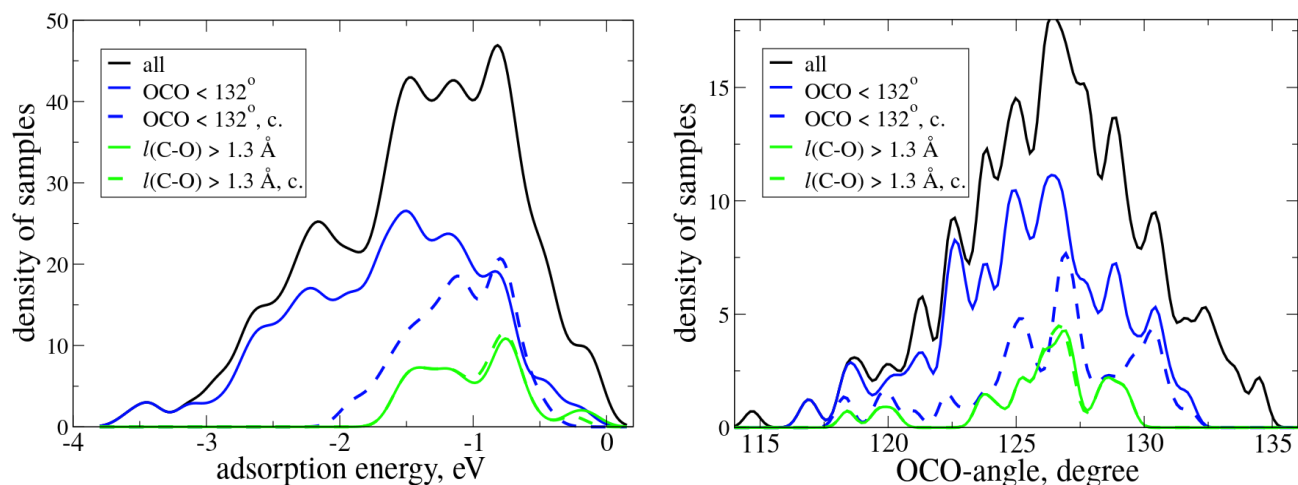


**Figure 2. Distribution of adsorption energies (left) and OCO-angles (right).** The distribution is shown for the whole data set (black), for the top subgroups of sites with  $\text{OCO} < 132^\circ$  angles (blue) and  $l(\text{C-O}) > 1.30 \text{ \AA}$  (green). The subgroups obtained with adsorption energy constraint are marked with “c.” and shown with dashed lines. The adsorption energy  $E_{\text{ads}}$  is defined as the difference between the total energy of the slab with adsorbed  $\text{CO}_2$  and the sum of total energies of the clean slab and an isolated  $\text{CO}_2$  molecule.

First we consider materials with the sites from subgroups obtained by minimization of OCO-angle without Sabatier principle constraint.<sup>27</sup> For quite many materials from these subgroups, independent on the cutoff value, there are no reports of successful  $\text{CO}_2$  conversion, even when they are used as supports for metal nanoparticles (Table 3). This is explained by the fact that absolute adsorption energies for these materials are above 2 eV (Fig. 2 left, Supplementary Table 4), indicating that their surfaces will be permanently poisoned by carbonate species at low or intermediate temperatures. This means that on materials with these sites hardly any reaction of  $\text{CO}_2$  conversion can proceed at low, especially room temperature. Moreover, as shown in Table 3, even at increased temperatures, 700-750 °C, the activity of these materials is low. Some of them have been considered as candidates for carbon capture and storage ( $\text{CaO}$ ,  $\text{SrO}$ ,  $\text{BaO}$ ,  $\text{Na}_2\text{O}$ )<sup>49</sup>, which implies formation of stable carbonates rather than  $\text{CO}_2$  transformation. Thus, we conclude that OCO-angle alone is not a good indicator of enhanced catalytic activity in  $\text{CO}_2$  conversion.

On the other hand, several of the materials with sites from  $l(\text{C-O}) > 1.30 \text{ \AA}$  subgroups (independent on either with or without Sabatier principle constraint) are known as good materials for  $\text{CO}_2$  conversion (Table 3) in different reactions proceeding at room or higher temperatures. For these sites, the absolute adsorption energies already satisfy the Sabatier principle (Fig. 2, left), as discussed above. We note that, contrary to what one may expect, there is no correlation between the adsorption energy and the value of  $l(\text{C-O})$  (see Supplementary Figure 5). Although there is a general trend, there are also significant variations in  $l(\text{C-O})$  for a given adsorption energy.

Interestingly, some of the materials with sites in the  $l(\text{C-O}) > 1.30 \text{ \AA}$  subgroups were studied as supports for metallic nanoparticles. For instance,  $\text{Ni/LaAlO}_3$  is a catalyst for dry reforming of methane<sup>48</sup> at  $700^\circ\text{C}$ . It was shown that its catalytic performance is higher in terms of  $\text{CO}_2$  and  $\text{CH}_4$  conversion rates compared to  $\text{Ni/La}_2\text{O}_3$  and  $\text{Ni/Al}_2\text{O}_3$ <sup>48</sup>. All sites on considered lanthanum (III) oxide surfaces belong to the subgroup of  $\text{OCO} < 132^\circ$  without Sabatier constraint, whereas the sites on  $\text{Al}_2\text{O}_3$  do not enter any of the two subgroups.  $\text{KNbO}_3$  has been studied only with Pt nanoparticles and as a composite with  $g\text{-C}_3\text{N}_4$  in photocatalytic reduction of  $\text{CO}_2$  into  $\text{CH}_4$ <sup>45,46</sup>.  $\text{Pt-KNbO}_3$  is  $\sim 2.5$  times more photoactive than  $\text{Pt-NaNbO}_3$ <sup>45</sup>, whereas the  $\text{NaNbO}_3$  is known to be photoactive even without nanoparticles<sup>47</sup>. This seems to suggest that  $l(\text{C-O})$  is a good indicator of  $\text{CO}_2$  activation for both unsupported and supported catalysts even at increased temperatures. Hence, the other materials with the sites from this subgroup are promising new candidates for this task. The most promising materials identified in this work are  $\text{CsNbO}_3$ ,  $\text{CsVO}_3$ ,  $\text{RbVO}_3$ ,  $\text{LaScO}_3$ ,  $\text{RbNbO}_3$ , and  $\text{NaSbO}_3$  as they have the sites from the larger  $l(\text{C-O})$  subgroups satisfying the above-mentioned criteria.

There is also a set of materials [ternaries  $A^{2+}B^{4+}\text{O}_3$  ( $A = \text{Ca, Sr, Ba}$ ,  $B = \text{Zr, Ti, Ge, Sn, Si}$ ) with a perovskite structure] containing both the surfaces with sites from the smaller  $\text{OCO}$  subgroups without Sabatier constraint and the surfaces with sites from the larger  $l(\text{C-O})$  subgroups (Table 3). These two types of sites are located on different surfaces. Thus, based on the above results, a material for which a surface with sites from the  $l(\text{C-O}) > 1.30 \text{ \AA}$  subgroups has lower formation

energy and is more abundant than the surface with sites from smaller OCO subgroups without Sabatier constraint is expected to be a good catalyst. To explore this possibility, we analyze the surfaces of these materials in more detail. Their most stable surfaces are AO-terminated (001) facets containing sites from the smaller OCO subgroup. The formation energies of  $ABO_3$ -terminated (110) surfaces with larger  $l(C-O)$  sites are higher: for  $BaZrO_3$ ,  $SrZrO_3$ ,  $CaZrO_3$ , and  $SrTiO_3$  the differences in formation energies are 0.049, 0.027, 0.013 and 0.037 eV/Å<sup>2</sup>, respectively. The zirconates and  $SrTiO_3$  were found to catalyze the water gas-shift reaction under increased temperatures, 700-1100 °C<sup>50</sup>. At room temperature the photocatalytic activity of  $SrTiO_3$  was found to be significantly decreased<sup>55</sup>. We attribute the latter finding to the strong carbonation of its most stable surface, which is consistent with the calculated high absolute value of CO<sub>2</sub> adsorption energy (-2.4 eV) for this surface. Thus, the activity of  $SrTiO_3$  at 700 °C and higher temperatures is consistent with the estimates of the CO<sub>2</sub> chemical potential given above. The difference in formation energies of the most stable CaO-terminated (001) surface and the stoichiometric (110) surface for  $CaTiO_3$  is less pronounced compared to zirconates and other titanates (CaO-terminated (001) is more stable than the (110) surface by only 0.009 eV/Å<sup>2</sup>). Thus, the (110) facets, which contain sites from the long  $l(C-O)$  subgroup, may be present on catalyst particles at the reaction conditions. This can explain the observed activity of  $CaTiO_3$  in CO<sub>2</sub> conversion not only at high but also at room temperature. We note that the activity of this material was also attributed to the presence of TiO<sub>2</sub> nanoparticles on the surface<sup>51</sup> at reaction conditions.

The OCO subgroup that includes most of the known good catalysts and a minimal number of inactive materials is  $OCO < 132^o$  with Sabatier principle. It contains the sites on discussed above  $LaAlO_3$ ,  $KNbO_3$  and  $NaNbO_3$  catalysts, but also on non-active  $YInO_3$  according to Ref. 44 (Table 3). This subgroup contains in addition the sites on a well-known CO<sub>2</sub> conversion catalyst  $Ga_2O_3$ . We should mention that catalytic activity of  $Ga_2O_3$  has been attributed to its reducibility. According to Pan and coworkers<sup>59</sup> CO<sub>2</sub> molecules are activated via dissociation on surface O-vacancies. However, in ref. 52 only one  $Ga_2O_3$  (100) surface was considered for which no energetically stable CO<sub>2</sub> chemisorption structures were

obtained with the PBE functional. We show in Supplementary Table 1 and Supplementary Figure 1 that this functional underestimates CO<sub>2</sub> adsorption energies. Moreover, in our study we considered also other surfaces and found stable CO<sub>2</sub> chemisorption structures on these surfaces. Thus, activation of CO<sub>2</sub> on Ga<sub>2</sub>O<sub>3</sub> can indeed proceed on O-atoms as discussed in our study, even without surface O vacancies. The subgroups with small OCO cutoffs, 123° and 124°, do not contain any sites on known active or non-active catalysts.

OCO < 132° subgroup with Sabatier principle contains a large number of sites with elongated C-O bonds. The overlap of this subgroup with  $l(\text{C-O}) > 1.30 \text{ \AA}$  subgroups is 19 samples (70% of the latter).

To demonstrate advantages of SGD over DTR in finding materials *genes* and their optimal combinations, we have done comparison of found SGD subgroups with DTR performance for  $l(\text{C-O})$ . DTR terminal nodes (leaves) with largest average  $l(\text{C-O})$  (Supplementary Figures 2 and 3) include surface sites on materials prone to extremely strong carbonation (Table 2), and also sites at which CO<sub>2</sub> prefers to physisorb, with  $l(\text{C-O}) = 1.17 \text{ \AA}$ . Also, one cannot check the effect of imposing the constraint as there is no standard way to mix regression and classification in DTR. Thus, DTR in contrast to SGD is not able to separate different activation modes and even fails sometimes in distinguishing activation from non-activation.

**Best materials for CO<sub>2</sub> reduction among calculated ones.** Now that good indicators of activation are identified (OCO with Sabatier principle and  $l(\text{C-O})$ ), all calculated materials can be ranked according to the value of these indicators (smaller OCO or larger  $l(\text{C-O})$  indicate C-O bond weakening and therefore higher catalytic activity, provided adsorption energy is moderate). The resulting list of most promising catalysts for CO<sub>2</sub> conversion is presented in Table 4. Each surface is characterized by maximum  $l(\text{C-O})$  and minimum OCO among all inequivalent sites on that surface. The materials with  $l(\text{C-O}) > 1.30 \text{ \AA}$  are listed in the order of decreasing  $l(\text{C-O})$ . Materials with OCO < 132° but  $l(\text{C-O}) < 1.30 \text{ \AA}$  are appended at the bottom of the list in the order of increasing OCO.

Materials and surface cuts higher up in the list in Table 4 that belong to both  $l(\text{C-O}) > 1.30 \text{ \AA}$  and OCO < 132° subgroups are the most promising catalysts,

followed by materials that belong to one of the subgroups, with the performance decreasing further down the list. Taking into account the number of active surface cuts and Sabatier principle, we conclude that  $\text{NaSbO}_3$  is the most promising unexplored catalyst for temperatures up to 340 °C (for  $\text{CO}_2$  pressures around 1 atm). Other  $A^{+1}B^{+5}\text{O}_3$  type promising materials are  $\text{KSbO}_3$  (for temperatures up to 110 °C) and  $\text{RbNbO}_3$  (up to 360 °C) that belong to both subgroups, and  $\text{LiSbO}_3$  (230 °C),  $\text{CsNbO}_3$  (260 °C),  $\text{CsVO}_3$  (110 °C),  $\text{NaVO}_3$  (130 °C), belonging to one of the subgroups (listed in the order of decreasing performance). There are also several promising  $A^{+3}B^{+3}\text{O}_3$  oxides with surfaces belonging to one or both subgroups, listed in the order they appear first time in the table:  $\text{ScAlO}_3$  (up to 550 °C),  $\text{GaAlO}_3$  (230 °C),  $\text{GaInO}_3$  (340 °C), rhombohedral  $\text{InAlO}_3$  (120 °C) – these and other In-containing materials are of course very expensive, but we list them here for completeness,  $\text{LaGaO}_3$  (210 °C),  $\text{ScGaO}_3$  (240 °C),  $\text{YAlO}_3$  (330 °C).

From the Table 4 it can be seen that not all promising materials belong to one of the found subgroups. This means that there are other optimal materials gene combinations that are not identified by SGD as statistically significant based on the current data set. Such combinations may be unique for a given material, or they may be found when more data for different materials are considered. Among these materials the most promising are:  $\text{InScO}_3$  (up to 430 °C),  $\text{MgSnO}_3$  (430 °C),  $\text{CaGeO}_3$  (570 °C), orthorhombic  $\text{InAlO}_3$  (230 °C),  $\text{CaSiO}_3$  (420 °C),  $\text{SrSiO}_3$  (460 °C),  $\text{SrGeO}_3$  (480 °C), and  $\text{BaSnO}_3$  (up to 550 °C).

## Discussion

We have developed the subgroup discovery strategy for finding improved oxide-based catalysts for the conversion of chemically inert molecules such as  $\text{CO}_2$  into useful chemicals or fuels. For this purpose we identified a new indicator of  $\text{CO}_2$  activation, namely the large C-O bond distance of the adsorbed molecule. This artificial-intelligence approach identifies the materials *genes* that correlate most strongly with the activation of the adsorbed molecule. Specifically these are the following clean surface properties: Hirshfeld charges of O atom at which  $\text{CO}_2$  adsorbs ( $q_0$ ) and of surface cations ( $q_{\min}$ ,  $q_{\max}$ ), surface geometric features [coordination descriptors  $Q_i$ ,  $i = 5, 6$ , distances between the surface O atom and

the nearest surface cations ( $d_i, i = 1-3$ ), electrostatic potential and electric field above the adsorption site ( $\Delta\phi, \phi_{2,6}$ ), polarizability and  $C_6$  coefficients for surface atoms ( $C_6^{\min}, C_6^0, \alpha_{\max}$ ), radii of HOMO and LUMO of the cation species ( $r_{+1}^{\max}, r_{+1}^{\min}, r_{\text{HOMO}}^{\min}$ ), ionization potential, electron affinity, and electronegativity of surface cation species ( $IP_{\max}, EA_{\max}, EN_{\min}$ ), features of O  $2p$  DOS ( $kurt, M, PC, U$ ), conduction band minimum (CBM), energies of the lowest unoccupied projected eigenstates of surface cation species ( $L_{\max}, L_{\min}$ ), and surface work function ( $W$ ). The found subgroup selectors predict whether a given candidate material belongs to the class of promising catalysts. The peculiarity of the large C-O bond indicator is that it automatically satisfies Sabatier principle for low and middle temperature  $\text{CO}_2$  conversion.

The present study shows also that the previously proposed indicator for  $\text{CO}_2$  activation, the decrease of the OCO angle<sup>27</sup>, is not appropriate and even correlates with a strong adsorption, so that poisoning by carbonation is likely which may be useful for carbon capture and storage (CCS) but not for carbon capture and utilization (CCU). When Sabatier principle is purposely included in the SGD search for small OCO, found subgroups substantially overlap with large  $l(\text{C-O})$  subgroups (70%), although still contain a few sites on inactive materials for  $\text{CO}_2$  conversion.

The subgroup analysis revealed an alternative mechanism of  $\text{CO}_2$  activation by adsorption, namely bonding of an O atom in  $\text{CO}_2$  with a surface cation(s), combined with only moderate electron transfer from the surface to the molecule, which results not only in reduction of OCO-angles, but also in pronounced elongation and weakening of the C-O bond. Although the latter can be achieved also by a larger charge transfer, it results in stronger binding of  $\text{CO}_2$  molecule to the surface and poisoning of the catalyst, contrary to the new mechanism. The same new mechanism is revealed when Sabatier principle is included when searching for small OCO subgroups.

We also demonstrated that a standard regression technique (DTR), which gives prediction models in a physically interpretable form similar to subgroup discovery (selectors based on identified descriptor), fails to identify the optimal combinations of materials *genes* and the activation in general. This failure is

traced back to the fact that DTR is a global approach, which minimizes error in prediction of the value of a target property for the whole data set. As a result, different combinations of *genes* leading to optimal value of the same target property are intermixed, and the combination that leads to the most optimal value is not identified. On the contrary, subgroup discovery finds unique local subsets in the data independent on the rest of the data. This makes it more suitable for identifying different combinations of materials *genes* that result in activation.

The other four considered potential indicators (charge at the adsorbed CO<sub>2</sub>, adsorption induced dipole moment, difference of charges on O-atoms and on C and O atoms of adsorbed CO<sub>2</sub>) were found to reproduce the results of SGD obtained for OCO-angles or C-O bond distances with significant overlap with corresponding subgroups.

Based on our results, we propose several new promising oxide-based catalysts for CO<sub>2</sub> conversion (Table 4). Although the present work has focused on oxides only, the overall strategy is general and can be applied to any other family of materials. This work also emphasizes the importance of documenting metadata and workflows for AI data analysis in materials science in order to ensure reproducibility of AI models and data analysis results.

## Methods

**Ab initio calculations.** The calculations are performed using density-functional theory (DFT) with the PBEsol exchange-correlation functional<sup>60</sup> as implemented in FHI-aims code<sup>61</sup> using ‘tight’ basis sets. The functional is chosen based on a comparison of calculated bulk lattice constants<sup>60</sup> and CO<sub>2</sub> adsorption energy to the available experimental results and high-level calculations (CCSD(T) and validated hybrid); see Supporting Information (SI) for more details on the computational setup. Nevertheless, it is expected that, because of the large set of systems inspected and the small variations introduced by the functional choice, the main trends will hold even when using another functional.

**Studied materials.** The data set includes 71 semiconductor oxide materials, with 141 surfaces. The materials are ternary ( $ABO_3$ ) and binary oxides with metal cations  $A$  and  $B$  from groups 1 to 5 (including La) and groups 12 to 15 of the periodic table. The full list of materials and surface cuts is given in Supplementary notes, and the data set is available in Ref. 26. In this study we considered only stoichiometric surface reconstructions obtained by atomic relaxation of stoichiometric bulk-like initial surface geometries. While this seems to be a limitation, our results show that indicators of activation calculated with this assumption correlate with experimental activity for known good oxide catalysts. This does not imply that surfaces of these materials do not reconstruct, but that the properties of unreconstructed surfaces can be used as descriptors for catalysis at reconstructed and defected surfaces under realistic conditions. Inclusion of surface reconstructions in the training data will further improve the predictions and will be a subject of future work.

**The details of SGD.** The SGD was done with the RealKD code (<https://bitbucket.org/realkd/>), modified to include quality functions described by eq. (1) and (2) in which the information gain was defined as:

$$u(p) = 1 - \left( \frac{-1}{\ln 2} \right) (p \cdot \ln(p) + (1-p) \cdot \ln(1-p)) \quad (3)$$

here  $p$  is the number of samples in a subgroup within required adsorption energy range divided by the total number of samples in the subgroup. Since Shannon entropy is a symmetric parabola-like function around 0.5, we set here  $F(Z) = 0$  for

$p \leq 0.5$ . Also,  $x \cdot \ln(x) = 0$  for  $x = 0$ . The search of subgroups is performed using a Monte Carlo scheme adapted for these tasks <sup>34</sup>.

The cut-off values  $x, y, \dots$  used for setting propositions (feature-1  $< x$ , feature-2  $\geq y$ , etc.) are obtained by  $k$ -means clustering, as implemented within RealKD. That is, for a desired number  $n = k - 1$  of cut-off values a set of  $k$  representative values of a given feature and  $k$  groups (clusters) of the data points are determined that minimize the deviation of all the feature values from the representative values. Thus, each value of the feature in the data set is assigned to a particular cluster, and the cut-offs are determined as the arithmetic mean between the closest feature values in neighboring clusters. The number  $k$  is a parameter, and different  $k$ -values can in principle result in different cut-off values. It is worth noting that, due to the stochastic Monte-Carlo sampling, the exact definitions of the subgroups may vary for consecutive runs of the SGD algorithm. We have tested  $k = 12, 14,$  and  $16$  and rerun the algorithm several times for each  $k$ . While the results indeed depend on the run and on the  $k$  value, the subgroups maximizing the quality function have largely or entirely overlapping populations, and selectors with the same or similar propositions. Here we report selectors that appear most often and have a high population and quality function values.

**Decision-tree regression.** The DTR analysis was performed using Python scikit-learn libraries. DTR is a supervised learning method in which the training set is repeatedly split into patterns (so called leaves) by means of propositions built from primary features. The fitting of a model is done with respect to the cost function, which encloses the deviation of fitted values of a target property from the actual values. In this study we considered two cost functions - mean squared error (MSE) and mean absolute error (MAE). The search of the most optimal partitioning (the so-called tree) is done with the greedy algorithm. To obtain the most optimal TR model, we used a standard approach for supervised machine learning - leave-one-out cross-validation with respect to the hyperparameters - minimal size of a leaf, maximal depth. Minimal size of a leaf is a bottom threshold of the population of a pattern, since too small size might result in overfitting. Maximal depth is a limit for the maximal number of splits in a tree.

## References

1. Arakawa, H. et al. Catalysis research of relevance to carbon management: progress, challenges, and opportunities. *Chem. Rev.* **101**, 953–996 (2001).
2. Olah, G.A. Beyond oil and gas: the methanol economy. *Angew. Chem. Int. Ed.* **44**, 2636–2639 (2005).
3. Olah, G.A., Goeppert, A. & Surya Prakash, G.K. Chemical recycling of carbon dioxide to methanol and dimethyl ether: from greenhouse gas to renewable, environmentally carbon neutral fuels and synthetic hydrocarbons. *J. Org. Chem.* **74**, 487–498 (2009).
4. Martens, J. A. et al. The Chemical Route to a Carbon Dioxide Neutral World. *ChemSusChem.* **10**, 1039-1055 (2017).
5. Klankermayer, J., Wesselbaum, S., Beydoun, K. & Leitner, W. Selective catalytic synthesis using the combination of carbon dioxide and hydrogen: catalytic chess at the interface of energy and chemistry. *Angew. Chem. Int. Ed.* **55**, 7296-7343 (2016).
6. Artz, J. et al. Sustainable conversion of carbon dioxide: an integrated review of catalysis and life cycle assessment. *Chem. Rev.* **118**, 434-504 (2018).
7. Li, W. et al. A short review of recent advances in CO<sub>2</sub> hydrogenation to hydrocarbons over heterogeneous catalysts. *RSC Adv.* **8**, 7651-7669 (2018).
8. Singh, A. K., Montoya, J. H., Gregoire, J. M. & Persson, K. A. Robust and synthesizable photocatalysts for CO<sub>2</sub> reduction: a data-driven materials discovery. *Nat. Commun.* **10**, 443 (2019).
9. Somorjai, G.A. & Li, Y. Introduction to Surface Chemistry and Catalysis, 2nd Edition. John Wiley & Sons. 1-800 (2010).
10. Nørskov, J.K., Studt, F., Abild-Pedersen, F. & Bligaard, T. Fundamental Concepts in Heterogeneous Catalysis (2014).
11. Thornton, A.W., Winkler, D. A., Liu, M. S., Haranczyk, M. & Kennedy, D. F. Towards computational design of zeolite catalysts for CO<sub>2</sub> reduction. *RSC Adv.* **5**, 44361 (2015).
12. Duyar, M.S. et al. Discovery of a highly active molybdenum phosphide

catalyst for methanol synthesis from CO and CO<sub>2</sub>. *Ang. Chem. Int. Ed.* **57**, 15045–15050 (2018).

13. Peterson, A.A. & Nørskov, J. K. Activity Descriptors for CO<sub>2</sub> Electroreduction to Methane on Transition-Metal Catalysts. *J. Phys. Chem. Lett.* **3**, 251–258 (2012).

14. Liu, X. et al. Understanding trends in electrochemical carbon dioxide reduction rates. *Nat. Commun.* **8**, 15438 (2017).

15. Schlexer Lamoureux, P. et.al. Machine learning for computational heterogeneous catalysis. *ChemCatChem.* **11**, 3581-3601 (2019).

16. Kitchin, J.P. Machine learning in catalysis. *Nat. Catal.* **4**, 230-232 (2018).

17. Medford, A.J., Kunz, M.R., Ewing, S.M., Borders & T., Fushimi, R. Extracting knowledge from data through catalysis informatics. *ACS Catal.* **8**, 7403-7429 (2018).

18. Foppa, L. et al. Materials genes of heterogeneous catalysis from clean experiments and artificial intelligence. arXiv:2102.08269v.

19. Kondratenko, E.V., Mul, G., Baltrusaitis, J., Larrazábal, G.O. & Pérez-Ramírez, J. *Energy Environ. Sci.* **6**, 3112 (2013).

20. Li, J. et al. *ACS Catal.* **9**, 10426 (2019).

21. Frei, M.S., Mondelli, C., Short, M.I.M. & Pérez-Ramírez, J. *ChemSusChem.* **13**, 6330 (2020).

22. Martin, O. et al. *Angew. Chem. Int. Ed.* **55**, 6261 (2016).

23. Richter, N.A., Sicolo, S., Levchenko, S.V., Sauer, J. & Scheffler, M. Concentration of vacancies at metal-oxide surfaces: case study of MgO(100). *Phys. Rev. Lett.* **111**, 045502 (2013).

24. Arndt, S. et al. A critical assessment of Li/MgO-based catalysts for the oxidative coupling of methane. *Cat. Rev. Sci. Eng.* **53**, 424-514 (2011).

25. Yan, Z., Chinta, S., Mohamed, A. A., Fackler, J. P. & Goodman, D. W. The role of f-centers in catalysis by Au supported on MgO. *J. Am. Chem. Soc.* **127**, 1604-1605 (2005).

26. <https://nomad-lab.eu/services/AIToolkit> → Subgroup discovery for carbon-dioxide activation

27. Freund, H.-J. & Roberts M. W. Surface chemistry of carbon dioxide. *Surf. Sci.*

Rep. **25**, 225-273 (1996).

28. Austin, N., Butina, B. & Mpourmpakis, G. *Progress in Natural Science: Materials International*. **26**, 487-492 (2016).

29. Hirshfeld, F.L. Bonded-atom fragments for describing molecular charge densities. *Theor. Chim. Acta*, **44**, 129-138 (1977).

30. Wrobel, S. An algorithm for multi-relational discovery of subgroups. *European Symposium on Principles of Data Mining and Knowledge Discovery (Springer)*. 78-87 (1997).

31. Friedman, J. H. & Fisher, N. I. Bump hunting in high-dimensional data. *Statistics and Computing*. **9**, 123-143 (1999).

32. Atzmueller, M.. Subgroup discovery, *Data Min. Knowl. Disc.* **5**, 35-49 (2015).

33. Boley, M., Goldsmith, B., Ghiringhelli, L. M. & Vreeken, J. Identifying consistent statements about numerical data with dispersion-corrected subgroup discovery. *Data Min. Knowl. Disc.* **31**, 1391-1418 (2017).

34. Goldsmith, B., Boley, M., Vreeken, J., Scheffler, M. & Ghiringhelli, L. M. Uncovering structure-property relationships of materials by subgroup discovery. *New J. Phys.* **19**, 013031 (2017).

35. Xu, Z. & Kitchin, J.R. *Catal. Commun.* **52**, 60 (2014).

36. Capdevila-Cortada, M., Vilé, G., Teschner, D., Pérez-Ramírez, J. & López, N. Reactivity descriptors for ceria in catalysis. *Appl. Catal. B: Envir.* **197**, 299-312 (2016).

37. Esterhuizen, J.A., Goldsmith, B. & Linic, S. Uncovering electronic and geometric descriptors of chemical activity for metal alloys and oxides using unsupervised machine learning. *Chem Catalysis*. **1**, 923-940 (2021).

38. Xu, W., Andersen M. & Reuter, K. Data-driven descriptor engineering and refined scaling relations for predicting transition metal oxide reactivity. *ACS Catal.* **11**, 734-742 (2021).

39. Grasselli, R.K. Fundamental principles of selective heterogeneous oxidation catalysis. *Top. Catal.* **21**, 79-88 (2002).

40. Stull, D.R. & Prophet, H. JANAF thermochemical tables. *J. Phys. Chem.* **78**, 2496-2506 (1974).

41. Wang, W. & Gong, J. Methanation of carbon dioxide: an overview. *Front. Chem. Sci. Eng.* **5**, 2-10 (2011).
42. Breiman, L., Friedman, J., Olshen, R. & Stone, C. Classification and regression trees. Wadsworth, New York (1984).
43. Novak, P.K., Lavrač, N. & Webb, G.I. Supervised descriptive rule discovery: A unifying survey of contrast set, emerging pattern and subgroup mining. *J. Mach. Learn. Res.* **10**, 377-403 (2009).
44. Khraisheh, M., Khazndar, A. & Al-Ghouti, M.A. Visible light-driven metal-oxide photocatalytic CO<sub>2</sub> conversion. *Int. J. Energy Res.* **39**, 1142-1152 (2015).
45. Shi, H. & Zou, Z. Photophysical and photocatalytic properties of ANbO<sub>3</sub> (A=Na, K) photocatalysts. *J. Phys. and Chem. Sol.* **73**, 788-792 (2012).
46. Shi, H., Zhang, C., Zhou, C. & Chen, G. Conversion of CO<sub>2</sub> into renewable fuel over Pt-g-C<sub>3</sub>N<sub>4</sub>/KNbO<sub>3</sub> composite photocatalyst. *RSC Adv.*, **5**, 93615-93622 (2015).
47. Fresno, F. et al. CO<sub>2</sub> reduction over NaNbO<sub>3</sub> and NaTaO<sub>3</sub> perovskite photocatalysts. *Photochem. Photobiol. Sci.*, **16**, 17-23 (2017).
48. Kathiraser, Y., Thitsartarn, W., Sutthiumporn, K. & Kawi, S. Inverse NiAl<sub>2</sub>O<sub>4</sub> on LaAlO<sub>3</sub>-Al<sub>2</sub>O<sub>3</sub>: unique catalytic structure for stable CO<sub>2</sub> reforming of methane. *J. Phys. Chem. C* **117**, 8120-8130 (2013).
49. Dunstan, M. T. et al. Large scale computational screening and experimental discovery of novel materials for high temperature CO<sub>2</sub> capture. *Energy Environ. Sci.* **9**, 1346-1360 (2016).
50. Saito, Y. *Patent No.:* US 8,540,898 B2; Sep. 24 (2013).
51. Sub Kwak, B. & Kang, M. Photocatalytic reduction of CO<sub>2</sub> with H<sub>2</sub>O using perovskite Ca<sub>x</sub>Ti<sub>y</sub>O<sub>3</sub>. *Appl. Surf. Sci.* **337**, 138-144 (2015).
52. Muroyama, H. et al. Carbon dioxide methanation over Ni catalysts supported on various metal oxides. *J. Catal.* **343**, 178-184 (2016).
53. Zhang, Z., Verykios, X. E., MacDonald, S. M. & Affrossman, S. Comparative study of carbon dioxide reforming of methane to synthesis gas over Ni/La<sub>2</sub>O<sub>3</sub> and conventional nickel-based catalysts. *J. Phys. Chem.* **100**, 744-754 (1996).
54. Lee, J. H. Cost-effective and dynamic carbon dioxide conversion into

- methane using a CaTiO<sub>3</sub>@Ni-Pt catalyst in a photo-thermal hybrid system. *J. Photochem. Photobiol. A: Chem.* **364**, 219-232 (2018).
55. Zeng, S., Kar, P., Thakur, U. K. & Shankar, K. A review on photocatalytic CO<sub>2</sub> reduction using perovskite oxide nanomaterials. *Nanotechnology* **29**, 052001 (2018).
56. Sekimoto, T. Electrochemical application of Ga<sub>2</sub>O<sub>3</sub> and related materials: CO<sub>2</sub>-to-HCOOH conversion. *Jpn. J. Appl. Phys.* **55**, 1202 (2016).
57. Teramura, K., Tsuneoka, H., Shishido, T. & Tanaka, T. Effect of H<sub>2</sub> gas as a reductant on photoreduction of CO<sub>2</sub> over a Ga<sub>2</sub>O<sub>3</sub> photocatalyst. *Chem. Phys. Lett.* **467**, 191-194 (2008).
58. Tang, S. et al. CO<sub>2</sub> Reforming of Methane to Synthesis Gas over Sol-Gel-made Ni/γ-Al<sub>2</sub>O<sub>3</sub> Catalysts from Organometallic Precursors. *J. Catal.* **194**, 424-430 (2000).
59. Pan, Y.-X., Liu, C.-J., Mei, D. & Ge, Q. Effects of hydration and oxygen vacancy on CO<sub>2</sub> adsorption and activation on β-Ga<sub>2</sub>O<sub>3</sub>(100). *Langmuir* **26**, 5551 (2010).
60. Perdew, J.P. et al. Restoring the density-gradient expansion for exchange in solids and surfaces. *Phys. Rev. Lett.* **100**, 136406 (2008).
61. Blum, V. et al. Ab initio molecular simulations with numeric atom-centered orbitals. *Comput. Phys. Comm.* **180**, 2175-2196 (2009).

## Acknowledgements

We thank Mario Boley for fruitful discussions on SGD and for providing the RealKD (for SGD) code. We also thank Yoshi Tateyama and Xinyi Lin for helping to generate the bulk oxide models and Helena Muñoz Galan and Oriol Lamiel Garcia for preliminary calculations. This project has received funding from the European Union's Horizon 2020 research and innovation program (#951786: The NOMAD European Center of Excellence and the ERC grant #740233: TEC1p), the Spanish MICIUN/FEDER RTI2018-095460-B-I00 and *María de Maeztu* MDM-2017-0767 grants and, in part, by *Generalitat de Catalunya* 2017SGR13 grant, plus a generous allocation of computational time provided by the *Red Española de*

*Supercomputación* - RES (QCM-2017-3-0006, QCM-2017-2-0005, QCM-2016-3-0005, QCM-2016-2-0007), and was supported by FAIRmat (FAIR Data Infrastructure for Condensed-Matter Physics and the Chemical Physics of Solids), DFG #460197019. The development of SGD approach was supported by Russian Science Foundation under grant 21-13-00419.

### Author contributions

M.S. and F.I. suggested the specific scientific problem and the general idea on methodology, A.M., Y.W., R.V. and F.V. generated the dataset, S.V.L. developed SGD methodology and modified the RealKD code, A.M. applied AI methodology to analyze the data, A.M., S.V.L., L.M.G. and M.S. interpreted the results, A.M., L.M.G., S.V.L., and M.S. established the Jupyter notebook, A.M., S.V.L. and L.M.G. wrote the manuscript.

### Data availability

The data set is available in the NOMAD AI Toolkit<sup>26</sup>.

### Code availability

A Jupyter notebook is available in the NOMAD AI Toolkit<sup>26</sup>.

### Competing interests

The authors declare no competing interests.

Table 1. Features that appear in the top SGD selectors (see text).

symbol	Meaning
$IP_{\min/\max}$	ionization potential, minimal and maximal in the pair of atoms <i>A</i> and <i>B</i> ; calculated as $E_{\text{atom}} - E_{\text{cation}}$
$EA_{\min/\max}$	electron affinity, minimal and maximal in the pair of atoms <i>A</i> and <i>B</i> ; calculated as $E_{\text{anion}} - E_{\text{atom}}$
$EN_{\min/\max}$	Mulliken electronegativity, minimal and maximal in the pair of gas-phase atoms <i>A</i> and <i>B</i>
$r_{-1}^{\min}, r_{-1}^{\max}$	radii of the maximum value of the Kohn-Sham radial wave functions of the spin-unpolarized spherically symmetric atom for HOMO-1, maximum (max) and minimum (min) in the pair of atoms <i>A</i> and <i>B</i>
$r_{+1}^{\min}, r_{+1}^{\max}$	radii of the maximum value of the Kohn-Sham radial wave functions of the spin-unpolarized

	spherically symmetric atom for LUMO, maximum (max) and minimum (min) in the pair of atoms <i>A</i> and <i>B</i>
<i>M</i>	energy at which the surface O 2 <i>p</i> -band projected density of states (PDOS) is maximal
<i>d</i> <sub>1</sub> , <i>d</i> <sub>2</sub> , <i>d</i> <sub>3</sub>	distances from surface O-atom to the first-, second-, and third-nearest cations
<i>W</i>	work function <i>W</i> , as the negative of the valence band maximum ( <i>W</i> = - <i>VBM</i> ) with respect to vacuum level
<i>q</i> <sub>min</sub> , <i>q</i> <sub>max</sub>	minimal and maximal Hirshfeld charges of cations in the pair <i>A</i> and <i>B</i> , calculated as an average for all surface cations of a given type
$\Delta$	band gap
<i>CBM</i>	conduction band minimum
<i>Q</i> <sub>5</sub> , <i>Q</i> <sub>6</sub>	local-order parameter with <i>l</i> = 5 or 6
<i>PC</i>	weighted surface O 2 <i>p</i> -band center
$\alpha_0$ , <i>C</i> <sub>6</sub> <sup>0</sup>	polarizability and <i>C</i> <sub>6</sub> -coefficient for surface O-atom obtained from many-body dispersion scheme
$\alpha_{\min}$ , $\alpha_{\max}$ , <i>C</i> <sub>6</sub> <sup>min</sup> , <i>C</i> <sub>6</sub> <sup>max</sup>	polarizability and <i>C</i> <sub>6</sub> -coefficient for cations, minimal and maximal in the pair <i>A</i> and <i>B</i> , calculated as an average for all surface cations of a given type
<i>q</i> <sub>0</sub>	Hirshfeld charge of O-atom at the surface
<i>wid</i>	square-root of the second moment of surface O 2 <i>p</i> -band
<i>wid</i> <sub>min</sub> , <i>wid</i> <sub>max</sub>	square root of the second moment of PDOS of cations within valence band, minimal and maximal in the pair <i>A</i> and <i>B</i> , calculated as an average for all surface cations of a given type
<i>C</i> <sub>min</sub> , <i>C</i> <sub>max</sub>	first moment for PDOS of cation within valence-band, minimal and maximal in the pair <i>A</i> and <i>B</i> , calculated as an average for all surface cations of a given type
$\varphi_{1.4}$ , $\varphi_{2.6}$ , $\varphi_{1.4} - \varphi_{2.6}$	electrostatic potentials above surface O-atom at 1.4 and 2.6 Å and their difference. 1.4 Å corresponds to the average length of the bond between C and surface O, 2.6 Å is the minimal distance from surface O to C-atom of physisorbed carbon-dioxide molecule as observed from our calculations
<i>L</i> <sub>min</sub> , <i>L</i> <sub>max</sub>	energy of lowest unoccupied projected eigenstate of surface cations, minimal and maximal in the pair <i>A</i> and <i>B</i> , calculated as an average for all surface cations of a given type
<i>kurt</i>	kurtosis of surface O 2 <i>p</i> -band PDOS
<i>U</i>	eigenstate with least negative value in surface O 2 <i>p</i> -band
<i>BV</i>	bond-valence value of surface O-atom

Table 2. Top subgroups and their selectors obtained by minimization of OCO-angle and maximization of *l*(C-O) with/out Sabatier principle (energies are in eV, distances are in Å, charges are in units of absolute electron charge, polarizabilities are in Bohr<sup>3</sup>). Proposition replacements that do not change the support are shown in parentheses.

cutoff	size	selector	cutoff	size	selector
--------	------	----------	--------	------	----------

OCO minimization without Sabatier principle constraint			OCO minimization with Sabatier principle constraint		
126	19	$L_{\max} > -2.70$ ( $L_{\min} > -2.19$ , $CBM > -3.40$ , $r_{+1}^{\max} \leq 2.83$ , $W < 5.80$ , $U > -5.61$ ) $IP_{\max} \geq -6.05$ $\alpha_{\max} \leq 184.5$ $\Delta\phi > 1.33$ $q_{\max} \leq 0.59$ $wid \leq 1.59$ $wid \geq 0.58$	126	15	$L_{\min} \geq -5.1085$ $\phi_{2.6} \leq 0.3033$ $\Delta\phi \leq 1.0622$ ( $c_{\max} \leq -8.5915$ ) $d_1 \geq 1.82$ $d_2 \geq 2.005$ $r_{+1}^{\max} > 2.83$
128	44	$EA_{\max} \geq -0.43$ $Q_6 \geq 0.51$ $\alpha_{\max} \geq 50.4$ ( $C_6^{\max} \geq 389.5$ , $\alpha_0 \leq 2.70$ ) $\Delta\phi \geq 1.00$ $q_{\min} \leq 0.49$	128	30	$C_6^{\min} \geq 369.5$ $L_{\max} \geq -4.73$ ( $r_{+1}^{\min} \leq 2.82$ , $IP_{\min} \leq -5.83$ , $r_{\text{HOMO}}^{\min} \leq 1.41$ ) $Q_5 \leq 0.83$ $\Delta\phi \geq 0.60$ $r_{+1}^{\max} \geq 2.80$ $C_6^0 \leq 12.10$
130	77	$L_{\max} \geq -5.23$ $EA_{\max} \leq 0.16$ ( $C_6^{\max} \geq 389.5$ , $IP_{\max} \geq -7.00$ ) $d_1 \geq 1.82$ $d_2 > 2.10$	130	40	$\phi_{2.6} \geq -0.15$ $\Delta\phi \geq 0.73$ $d_1 \leq 2.01$ $d_2 \geq 1.96$ $d_3 \geq 2.025$ ( $c_{\min} \leq -9.07$ , $W \geq 5.10$ ) $q_{\min} \leq 0.49$ $r_{+1}^{\min} \geq 1.94$
132	139	$IP_{\max} \geq -6.99$ $q_0 \leq -0.32$ $C_6^0 \geq 10.36$	132	58	$q_0 \leq -0.3386$ $M \leq -6.292$ $kurt \geq 2.1035$ $IP_{\max} \geq -6.2085$ $r_{\text{HOMO}}^{\min} \leq 1.407$ ( $IP_{\min} \leq -5.91$ , $r_{+1}^{\min} \leq 2.82$ )
I(C-O) maximization without Sabatier principle constraint			I(C-O) maximization with Sabatier principle constraint		
1.26	121	$C_6^{\min} \geq 343.5$ $\phi_{2.6} \leq 0.66$ $Q_5 \leq 0.83$ $M \geq -8.05$ ( $PC \geq -9.32$ )	1.26	56	$CBM \geq -5.17$ ( $L_{\min} \geq -5.11$ ) $\Delta\phi \leq 1.13$ $PC \geq -8.62$ $d_3 \leq 2.48$ $M \leq -6.06$
1.28	38	$EA_{\max} \leq 0.005$ $d_2 > 2.22$ $M \leq -4.12$	1.28	30	$W \geq 5.10$ ( $M \leq -5.19$ , $U \leq -4.92$ , $PC \leq -7.21$ ) $d_2 > 2.14$ $q_{\min} < 0.48$
1.30	27	$U \leq -5.34$ $d_2 > 2.14$ $q_{\min} < 0.48$ $kurt \geq 2.10$ ( $q_{\max} \geq 0.47$ )	1.30	27	$EA_{\max} \leq 0.005$ ( $W \geq 5.10$ , $M \leq -5.19$ , $U \leq -4.92$ , $PC \leq -7.21$ ) $EN_{\min} \leq -3.19$ ( $W \geq 5.10$ , $q_0 \geq -0.45$ , $c_{\max} \leq -7.18$ , $r_{\text{HOMO}}^{\min} \leq 1.41$ , $\phi_{1.4} \leq 2.40$ , $c_{\min} \leq -8.135$ , $q_{\max} \geq 0.47$ , $M \leq -5.19$ , $IP_{\min} \leq -5.91$ , $wid \geq 0.58$ , $U \leq -4.92$ , $r_{-1}^{\max} \geq 0.97$ , $PC \leq -7.21$ , $\Delta\phi \leq 1.81$ ) $d_2 > 2.14$ $q_{\min} < 0.48$ $kurt \geq 2.51$

Table 3. The catalytic performance of materials which contain the sites from larger  $I(\text{C-O})$  or/and smaller OCO subgroups.

material	catalytic reaction	CO <sub>2</sub> adsorption energies, eV	belong to subgroups
NaNbO <sub>3</sub>	photocatalytic CO <sub>2</sub> reduction with ~70% of CO selectivity <sup>45,47</sup>	-0.77 - -0.81	materials with sites from $I(\text{C-O}) > 1.30 \text{ \AA}$ subgroup and OCO < 132 <sup>o</sup> subgroup with Sabatier principle constraint
LaAlO <sub>3</sub>	dry reforming of methane with Ni-nanoparticles; performance is higher than for Ni-La <sub>2</sub> O <sub>3</sub> and Ni-Al <sub>2</sub> O <sub>3</sub> <sup>48</sup>	-1.17	
KNbO <sub>3</sub>	photocatalytic reduction of CO <sub>2</sub> into CH <sub>4</sub> as a composite with Pt/g-C <sub>3</sub> N <sub>4</sub> ; significant improvement of activity when compared to Pt/g-C <sub>3</sub> N <sub>4</sub> ; Pt-KNbO <sub>3</sub> is ~2.5 times more photoactive than Pt-NaNbO <sub>3</sub> <sup>45,46</sup>	-0.56 - -0.68	
CaTiO <sub>3</sub>	CO <sub>2</sub> hydrogenation under UV-irradiation, although activity is not very high <sup>51,54</sup> ; twice higher activity with Ni nanoparticles <sup>54</sup>	up to -2.70	materials with sites from $I(\text{C-O}) > 1.30 \text{ \AA}$ subgroups and from OCO < 132 <sup>o</sup> subgroup without Sabatier principle constraint
CaZrO <sub>3</sub> , SrZrO <sub>3</sub> , BaZrO <sub>3</sub> , SrTiO <sub>3</sub>	reverse water gas shift reaction (RWGS) under 700-1100 <sup>o</sup> C <sup>50</sup>	up to -2.75	
SrTiO <sub>3</sub>	photocatalytic CO <sub>2</sub> methanation with Pt, Au-nanoparticles, significant decrease of activity during reaction <sup>55</sup>	up to -2.40	
YInO <sub>3</sub> *	no activity observed in photocatalytic CO <sub>2</sub> conversion <sup>44</sup>	-1.16 - -1.47	
CaO, SrO, BaO, Na <sub>2</sub> O	strong carbonation, candidate materials for carbon capture and storage (CCS) <sup>49</sup>	-1.60 - -3.57	materials with sites only from OCO < 132 <sup>o</sup> subgroup without Sabatier principle constraint
La <sub>2</sub> O <sub>3</sub>	dry reforming of methane with supported Ni- nanoparticles; lower performance than on Ni-LaAlO <sub>3</sub> <sup>48</sup> and on some other supported catalysts <sup>52</sup> at 700 and 250 <sup>o</sup> C correspondingly	-2.14 - -3.11	
CaO	twice smaller reaction rate in CO <sub>2</sub> reforming of methane reaction with supported Ni nanoparticles than on Ni-La <sub>2</sub> O <sub>3</sub> <sup>53</sup> at 750 <sup>o</sup> C	-1.60 - -3.42	
Ga <sub>2</sub> O <sub>3</sub>	electrochemical reduction of CO <sub>2</sub> to formic acid <sup>56</sup> ; (photo)catalytic hydrogenation of CO <sub>2</sub> <sup>57</sup>	-0.74 - -1.34	materials with sites from OCO < 132 <sup>o</sup> subgroup with Sabatier principle constraint
Al <sub>2</sub> O <sub>3</sub>	dry reforming of methane with supported Ni- nanoparticles <sup>58</sup> ; lower performance than on Ni-LaAlO <sub>3</sub> <sup>48</sup>	-0.87	

\*material with sites also from OCO < 132<sup>o</sup> subgroup *with* Sabatier principle constraint

Table 4. Best materials and surface cuts for CO<sub>2</sub> activation according to the  $l(\text{C-O})$  and OCO indicators.

material	surface cut	$l(\text{C-O})$ , Å	OCO, degree	$E_{\text{ads}}$ , eV	in $l(\text{C-O}) > 1.30$ Å subgroup	in OCO < 132° c. subgroup
according to $l(\text{C-O})$ indicator						
NaSbO <sub>3</sub>	100	1.370	125.21	-1.32	yes	yes
Ga <sub>2</sub> O <sub>3</sub>	212	1.365	124.57	-1.34		yes
NaSbO <sub>3</sub>	010	1.365	125.95	-1.09	yes	yes
LiSbO <sub>3</sub>	010	1.359	126.66	-1.04		yes
NaNbO <sub>3</sub>	100	1.353	125.87	-0.78	yes	yes
ScAlO <sub>3</sub>	010	1.351	127.25	-1.18		yes
KSbO <sub>3</sub>	110	1.345	128.54	-0.72	yes	yes
LiNbO <sub>3</sub>	100	1.344	126.23	-0.87		
NaNbO <sub>3</sub>	010	1.344	126.85	-0.77	yes	yes
InScO <sub>3</sub>	121	1.342	126.26	-1.23		
CsNbO <sub>3</sub>	100	1.34	126.6	-0.87	yes	
RbNbO <sub>3</sub>	111	1.338	126.61	-1.37	yes	yes
CsNbO <sub>3</sub>	010	1.336	126.23	-1.11	yes	
MgSnO <sub>3</sub>	100	1.334	119.84	-1.58		
GaAlO <sub>3</sub>	100	1.332	129.12	-1.02		yes
CaGeO <sub>3</sub>	001(GeO <sub>2</sub> -term.)	1.331	127.65	-0.75		
InAlO <sub>3</sub> -or.	121	1.33	130.09	-1.02		
ScAlO <sub>3</sub>	121	1.328	131.61	-0.86		
GaInO <sub>3</sub>	110	1.327	126.98	-1.34	yes	
LaAlO <sub>3</sub>	110	1.327	129.38	-1.17	yes	yes
CsVO <sub>3</sub>	110	1.327	126.1	-0.72	yes	
KNbO <sub>3</sub>	110	1.327	128.49	-0.68	yes	yes
RbVO <sub>3</sub>	110	1.326	126.04	-1.14		
Ga <sub>2</sub> O <sub>3</sub>	110	1.325	127.76	-1.09		yes
NaVO <sub>3</sub>	110	1.324	127.12	-0.755	yes	
NaNbO <sub>3</sub>	110	1.322	128.14	-0.805	yes	yes
InAlO <sub>3</sub> -rh.	110	1.318	126.83	-0.73	yes	yes
LaGaO <sub>3</sub>	100	1.317	125.29	-0.97	yes	
ScGaO <sub>3</sub>	010	1.314	124.68	-1.06		yes
GaInO <sub>3</sub>	120	1.313	118.41	-1.43	yes	yes
MgGeO <sub>3</sub> -tetr.	001(GeO <sub>2</sub> -term.)	1.312	126.18	-1.35		
ScAlO <sub>3</sub>	100	1.312	122.28	-1.89		yes
YAlO <sub>3</sub>	011	1.312	127.26	-1.18	yes	yes
InScO <sub>3</sub>	110	1.31	122.28	-1.54		yes
In <sub>2</sub> O <sub>3</sub>	111	1.309	128.44	-0.65		
InAlO <sub>3</sub> -or.	110	1.309	127.2	-0.66		yes
YAlO <sub>3</sub>	100	1.308	123.82	-1.305	yes	yes
InScO <sub>3</sub>	110(In <sub>2</sub> O <sub>3</sub> -term.)	1.305	124.92	-1.57		yes
YGaO <sub>3</sub>	100	1.305	124.76	-1.23		
In <sub>2</sub> O <sub>3</sub>	110	1.301	125.86	-1.00		
Sc <sub>2</sub> O <sub>3</sub>	111	1.301	130.43	-0.885		
LaGaO <sub>3</sub>	110	1.301	128.88	-0.83	yes	yes
LaScO <sub>3</sub>	100	1.301	123.6	-1.53	yes	
according to OCO indicator						
CaSiO <sub>3</sub>	001(CaO-term.)	1.290	118.84	-1.54		

SrSiO <sub>3</sub>	001(SrO-term.)	1.295	119.10	-1.66		
CaGeO <sub>3</sub>	001(CaO-term.)	1.288	120.88	-1.94		
Ga <sub>2</sub> O <sub>3</sub>	212	1.297	121.21	-1.53		
InScO <sub>3</sub>	110	1.292	121.23	-1.88		
InScO <sub>3</sub>	100	1.277	121.40	-1.74		
RbVO <sub>3</sub>	100	1.283	121.64	-0.53		
In <sub>2</sub> O <sub>3</sub>	110	1.280	122.52	-1.57		
InScO <sub>3</sub>	110(In <sub>2</sub> O <sub>3</sub> -term.)	1.284	122.80	-1.78		
SrGeO <sub>3</sub>	100(SrO-term.)	1.277	122.90	-1.70		
TiO <sub>2</sub> -rutile	100	1.276	123.61	-1.05		
ZrO <sub>2</sub>	111	1.280	123.72	-0.92		
BaSnO <sub>3</sub>	001(BaO-term.)	1.267	123.80	-1.89		
ScGaO <sub>3</sub>	110	1.292	123.85	-1.22		
ZrO <sub>2</sub>	011	1.264	124.06	-0.72		
LiVO <sub>3</sub>	110	1.295	124.76	-0.70		
NaNbO <sub>3</sub>	010	1.273	125.00	-1.66		
MgTiO <sub>3</sub>	012	1.295	125.16	-1.47		
InAlO <sub>3</sub> -or.	010	1.284	125.30	-0.82		yes
YInO <sub>3</sub>	100	1.293	125.69	-1.47		
KNbO <sub>3</sub>	010	1.277	125.97	-1.52		
InAlO <sub>3</sub> -or.	110	1.278	126.04	-0.90		
ScAlO <sub>3</sub>	110	1.277	126.10	-1.33		
Al <sub>2</sub> O <sub>3</sub>	012	1.265	126.46	-0.87		yes
Sc <sub>2</sub> O <sub>3</sub>	110	1.265	126.47	-1.14		
CaSiO <sub>3</sub>	110(CaO-term.)	1.278	126.49	-1.44		
LaInO <sub>3</sub>	100	1.287	127.13	-1.27		
Sc <sub>2</sub> O <sub>3</sub>	111	1.265	127.49	-0.95		
YInO <sub>3</sub>	110	1.298	127.61	-1.22		yes
ScAlO <sub>3</sub>	121	1.268	127.73	-0.755		
MgTiO <sub>3</sub>	001	1.265	127.85	-1.37		
BaGeO <sub>3</sub>	001(BaO-term.)	1.270	128.50	-1.80		
SrTiO <sub>3</sub>	001(TiO <sub>2</sub> -term.)	1.266	128.53	-1.92		
ZnO	10-10	1.270	128.60	-1.005		
YGaO <sub>3</sub>	110	1.263	128.68	-1.60		
SrSnO <sub>3</sub>	001(SnO <sub>2</sub> -term.)	1.273	128.90	-1.64		
Sc <sub>2</sub> O <sub>3</sub>	001	1.289	128.90	-1.70		
MgGeO <sub>3</sub>	001	1.260	128.93	-1.09		
CaO	001	1.262	129.20	-1.60		
Al <sub>2</sub> O <sub>3</sub>	001	1.283	129.22	-1.315		
BaSnO <sub>3</sub>	001(SnO <sub>2</sub> -term.)	1.270	129.50	-1.87		
CaSnO <sub>3</sub>	001(SnO <sub>2</sub> -term.)	1.272	130.09	-1.32		
KVO <sub>3</sub>	010	1.267	130.17	-0.55		
CaZrO <sub>3</sub>	101(ZrO <sub>2</sub> -term.)	1.265	130.36	-1.86		
CaSnO <sub>3</sub>	110(SnO <sub>2</sub> -term.)	1.272	130.50	-1.44		
SrGeO <sub>3</sub>	100(GeO <sub>2</sub> -term.)	1.270	130.90	-1.515		
CaTiO <sub>3</sub>	101(TiO <sub>2</sub> -term.)	1.266	131.42	-1.505		
SnO <sub>2</sub>	100	1.257	131.50	-0.85		
BaSiO <sub>3</sub>	100	1.243	131.60	-0.75		
MgO	111	1.296	131.70	-1.24		

**Figure 1. Correlation between the larger of the two C-O bond lengths and the OCO-angle for charged gas-phase and adsorbed CO<sub>2</sub>. The OCO-**

angle in charged gas-phase CO<sub>2</sub> is shown with the red line, and adsorbed CO<sub>2</sub> structures are shown with the dots. Colored dots: blue – adsorption sites from the unconstrained subgroup with OCO < 132°, green – subgroup of sites with l(C-O) > 1.30 Å, black – the remaining samples (see the text). The subgroups obtained with Sabatier principle constraint are marked with “c.”.

**Figure 2. Distribution of adsorption energies (left) and OCO-angles (right).** The distribution is shown for the whole data set (black), for the top subgroups of sites with OCO < 132° angles (blue) and l(C-O) > 1.30 Å (green). The subgroups obtained with adsorption energy constraint are marked with “c.” and shown with dashed lines. The adsorption energy  $E_{\text{ads}}$  is defined as the difference between the total energy of the slab with adsorbed CO<sub>2</sub> and the sum of total energies of the clean slab and an isolated CO<sub>2</sub> molecule.

## Supplementary Information.

### Artificial-intelligence-driven discovery of catalyst *genes* with application to CO<sub>2</sub> activation on semiconductor oxides

A. Mazheika<sup>1,\*</sup>, Y. Wang<sup>1</sup>, R. Valero<sup>2</sup>, F. Viñes,<sup>2</sup> F. Illas<sup>2</sup>, L. M. Ghiringhelli<sup>1</sup>, S. V. Levchenko<sup>3,1,\*</sup>,  
M. Scheffler<sup>1</sup>

<sup>1</sup>Fritz-Haber-Institut der Max-Planck-Gesellschaft, 14195 Berlin-Dahlem, Germany

<sup>2</sup>Departament de Ciència de Materials i Química Física and  
Institut de Química Teòrica i Computacional (IQTCUB),

Universitat de Barcelona, c/ Martí i Franquès 1, Barcelona 08028, Spain

<sup>3</sup>Skolkovo Institute of Science and Technology, Skolkovo Innovation Center, 3 Nobel Street,  
143026 Moscow, Russia

\*corresponding authors: [alex.mazheika@gmail.com](mailto:alex.mazheika@gmail.com), [mazheika@fhi-berlin.mpg.de](mailto:mazheika@fhi-berlin.mpg.de); [levchenko@fhi-berlin.mpg.de](mailto:levchenko@fhi-berlin.mpg.de)

## Supplementary methods

**Ab initio methods.** All *ab initio* calculations were performed with the all-electron full-potential electronic structure FHI-aims code package<sup>1</sup> using density-functional theory (DFT) and numerical atom-centered basis functions. The standard 'tight' settings (grids and basis functions) were employed<sup>1</sup>, which deliver the adsorption energies with basis-set superposition errors below 0.07 eV per adsorbed molecule. The exchange-correlation (XC) functional approximation was chosen based on a comparison to available experimental and high-level theoretical data on CO<sub>2</sub> adsorption energy (see below). PBE<sup>2</sup> and PBEsol<sup>3</sup> functionals with and without Tkatchenko-Scheffler (TS) pairwise dispersion-correction method<sup>4</sup> were tested. LDA<sup>5</sup> and RPBE<sup>6</sup> have been previously shown to give large errors for adsorption of CO<sub>2</sub><sup>7,8</sup>. All systems were treated as spin non-polarized. The bulk lattice vectors were calculated with the same exchange-correlation functional as the surface and the adsorbed molecule properties. The *k*-points for the bulk calculations were converged with respect to lattice vectors. The slabs were symmetric, and all atoms therein were allowed to relax. We did not constrain any side of a slab in order to have the same surface geometry on both sides, which is important for calculation of surface primary features. The slab thickness was also tested, and it was set to about 11 Å or larger in most cases, based on the convergence of the surface energy (within 5 meV/Å<sup>2</sup>) and the work function (within 10 meV) with respect to the thickness. For the surface supercells the *k*-grids were scaled from corresponding bulk grids. The lattice constants were obtained from the relaxed bulk unit cells. The initial geometries of adsorbed CO<sub>2</sub> before full atomic relaxation were obtained by placing the CO<sub>2</sub> molecule at different possible adsorption sites (metal and O sites, top, bridge, and hollow sites) and in different orientations (C down, O down) on one side of the slab. The size of the surface supercells was set based on test calculations, so that the interaction between the periodic images of the adsorbed CO<sub>2</sub> was below 0.1 eV. The resulting distance between the images of the C atom was about 8 Å. The adsorption of CO<sub>2</sub> has been considered only on one side of the slab, and a dipole correction<sup>9</sup> was included to prevent spurious electrostatic interactions. The lattice vector along the direction parallel to the vacuum gap was 200 Å. All atoms in the systems have been allowed to relax until the maximum remaining force fell below 10<sup>-2</sup> eV/Å.

There are few experimental data available for CO<sub>2</sub> adsorption at clean monocrystalline surfaces without impurities: at CaO (001)<sup>10</sup> and at ZnO (10-10)<sup>11,12</sup>. We compared the calculated adsorption energies ( $E_{\text{ads}}$ ) to the microcalorimetry and temperature programmed desorption (TPD) data. The adsorption energies were calculated as the difference between total energies of the slab with the adsorbed molecule, clean surface slab, and a free gas-phase CO<sub>2</sub> molecule. The calculations of the surfaces were performed with symmetric 5-atomic layer slabs for CaO (001) and 4 double-layer slab for ZnO (10-10). 8×8×8 and 10×10×6 *k*-point grids were used for cubic CaO and

hexagonal ZnO bulk unit cells, respectively. Surface unit cells were (2×2) for CaO (001), for ZnO (10-10) we considered two cells – (1×1) and (1×2).

The results for CaO (001) and ZnO (10-10) are shown in Supplementary Table 1. In the case of CaO the PBE adsorption energy is the closest to the experimentally observed value both from TPD and microcalorimetry, whereas PBEsol and PBEsol+TS values are closer to the one obtained with CCSD(T) using an embedded cluster model<sup>10</sup>. The inconsistency of the high-level theoretical and the experimental results was explained<sup>10</sup> by the formation of agglomerates of adsorbed CO<sub>2</sub> molecules even in ultrahigh vacuum. Relative to CCSD(T), PBEsol+TS performs better.

In the case of ZnO (10-10) the experimental data have been obtained for two adsorption coverages: 100% [(1×1) structure] and 50% [(1×2) structure]. In contrast to CaO, TPD and microcalorimetry values differ by about 0.2 eV (Supplementary Table 1). Taking into account that the calculated thermo-desorption energies depend on the chosen kinetic model as well as on the pre-exponential factor, we consider the microcalorimetry results as more accurate. The PBEsol adsorption energies match both measured values with the best accuracy (~0.1 eV). PBEsol+TS slightly overestimates the adsorption energies. This is not unexpected, since PBEsol functional behaves similarly to LDA for interatomic interactions at the middle-range distances, so that inclusion of additional vdW-correction leads to overestimation of binding energies. In addition, the TS scheme based on non-iterative Hirshfeld partitioning of the electron density was found to fail in predicting adsorption energies for some ionic systems, due to inaccurate description of polarizabilities<sup>13</sup>.

**Supplementary Table 1.** The experimental and theoretical energies of adsorption (in eV) of CO<sub>2</sub> at CaO (001) and ZnO (10-10) surfaces.

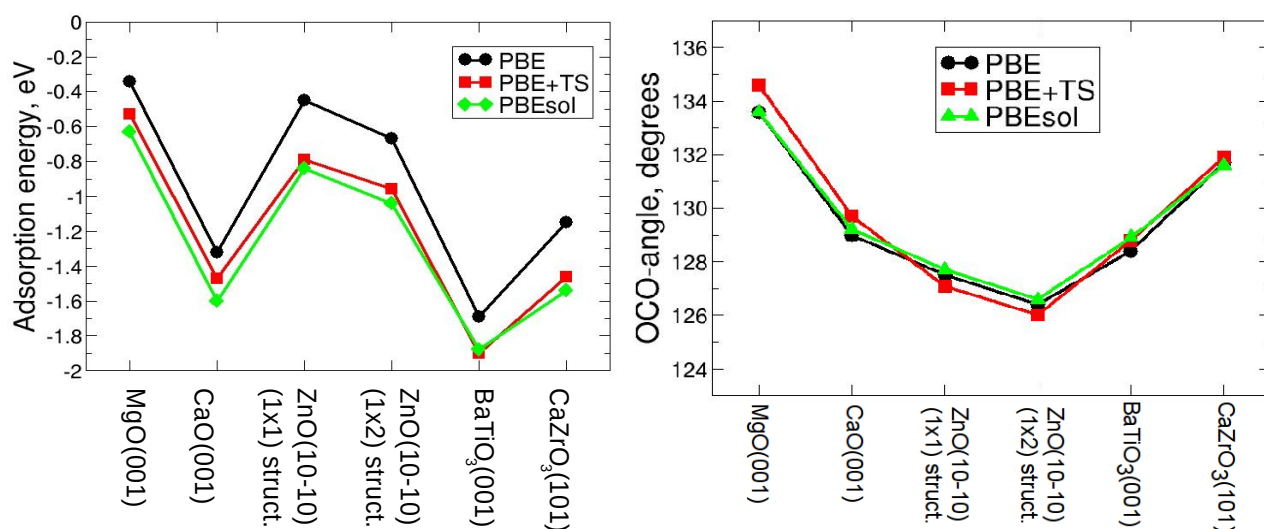
method	CaO (001)	ZnO (10-10)		MgO (001)
		(1×1) structure	(1×2) structure	
PBE	-1.32	-0.45	-0.67	-0.34
PBE+TS	-1.47	-0.79	-0.96	-0.53
PBEsol	-1.60	-0.84	-1.04	-0.63
PBEsol+TS	-1.75	-1.00	-1.19	-0.79
TPD	-1.24 – -1.45 [10]	-0.55 [11]	-0.90 [11,12]	-0.41 [14]
microcalorimetry	~ -1.30 [10]	-0.72 [12]	-1.12 [12]	-
high-level calculations	-1.91 ± 0.10 <sup>a</sup> [10]	-	-	-0.64 <sup>b</sup> [15]

<sup>a</sup>CCSD(T); <sup>b</sup>HSE(0.3)+vdW

We also compare the GGA CO<sub>2</sub> adsorption energies for MgO (001) surface with hybrid HSE(0.3)+vdW functional results<sup>15</sup>, where HSE(0.3)+vdW is the HSE functional with 30% fraction

of exact exchange plus the many-body dispersion correction<sup>16</sup>. This functional was shown to yield CO<sub>2</sub> adsorption energies very close to CCSD(T) for embedded clusters<sup>15</sup>, and the adsorption energy was found to be -0.64 eV. The closest value was obtained with the PBEsol functional (-0.63 eV). Thus, PBEsol compares favorably to both experiment and higher-level calculations. In addition to the above-mentioned systems, two more systems were tested: CO<sub>2</sub> adsorption on BaO-terminated BaTiO<sub>3</sub> (001) and on CaZrO<sub>3</sub> (101) surfaces. In general, we find that *relative differences* in adsorption energy between different XC approximations are weakly dependent on the material and surface termination (Supplementary Figure 1, left).

In addition to adsorption energies, another important parameter of CO<sub>2</sub> adsorption is the OCO angle, which is 180° in the neutral gas-phase molecule and close to 120° (as in a gas-phase CO<sub>3</sub><sup>2-</sup> ion) in adsorbed systems. As there are no precise experimental data like in the case of adsorption energies, here we rely on a weak sensitivity of the OCO angle to XC functional approximations. PBE, PBE+TS, and PBEsol provide very close OCO-angles for all tested systems (Supplementary Figure 1, right). The largest difference was observed in MgO (001) case where PBE+TS value is larger than PBE and PBEsol by 1.0°. In all other cases such deviation was 0.4 degree on average.

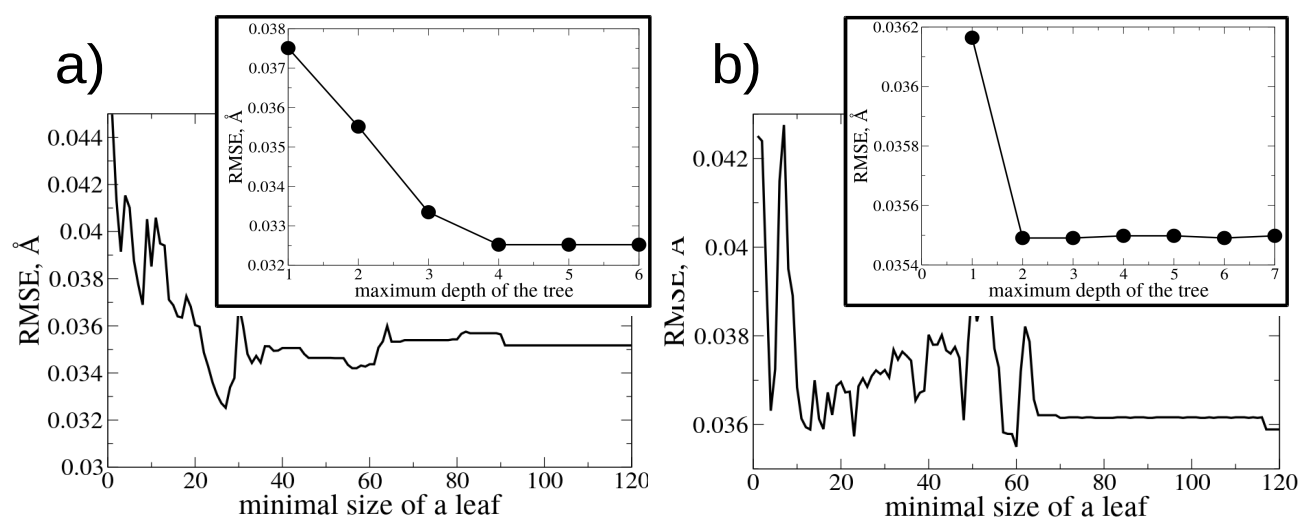


**Supplementary Figure 1.** The adsorption energies (left) and OCO-angles (right) of adsorbed CO<sub>2</sub> for different surfaces and XC functionals.

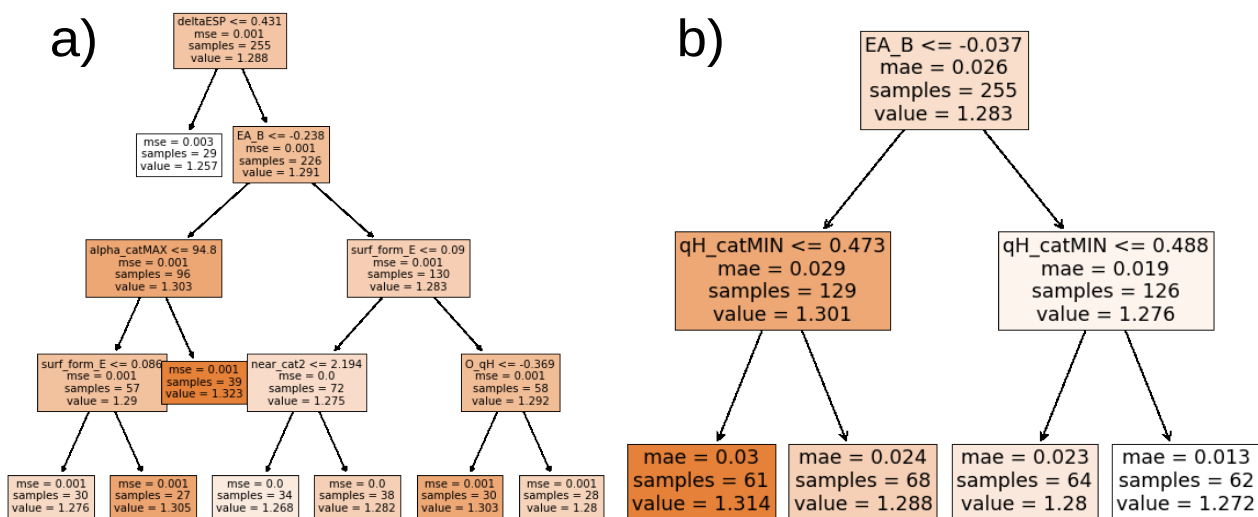
Summarizing the test results and taking into account that PBEsol provides a very good agreement between calculated and experimental bulk lattice constants for ionic solids<sup>3</sup>, we conclude that PBEsol is the best choice for our study. This result may be explained by the accuracy in prediction of lattice parameters in PBEsol<sup>17</sup> that results in a correct distribution of electronic density on surfaces.

**Decision tree regression models obtained for  $l(\text{C-O})$ .** We have done a comparison of found SGD subgroups with DTR performance for  $l(\text{C-O})$ . Two cost functions were used in DTR – mean absolute error (MAE) and mean squared error (MSE), and the patterns with largest average  $l(\text{C-O})$  values in each obtained tree were analyzed. We did not take into account the Sabatier principle explicitly in DTR, since there exists no standard decision tree algorithm wrapping regression and classification simultaneously. Thus, we do not consider DTR for OCO-angle.

The leave-one-out cross validation was used for the search of the optimal set of hyperparameters – minimal size of a leaf and maximum depth of the tree. The search was done on a grid at first for the minimal size of a leaf, then for selected local and global minima for maximum depth of the tree with fixed minimal sizes. The most optimal sets of hyperparameters {min. size, max. depth} are {27, 4} for  $l(\text{C-O})$  DTR model with MSE cost function and {60, 2} for  $l(\text{C-O})$  DTR model with MAE (Supplementary Figure 2). With these sets of hyperparameters the regression trees shown in Supplementary Figure 3 were obtained.



**Supplementary Figure 2.** The results of leave-one-out cross-validation for tree regression models with respect to the minimal size of a leaf and next the maximum depth of the tree (insets): a)  $l(\text{C-O})$  as the target with MSE as the cost function; b)  $l(\text{C-O})$  as the target with MAE as the cost function.



**Supplementary Figure 3.** The regression tree models obtained for a) OCO angle as the target with MSE as the cost function; b) OCO angle as the target with MAE as the cost function.

The DTR patterns with the largest mean value are dependent on which cost function is used. With MSE as cost function, the pattern with large  $l(\text{C-O})$  values is defined as ( $\text{EA}_{\text{max}} \leq -0.24$  eV) AND ( $\alpha_{\text{max}} > 94.80$ ) AND ( $\Delta\phi > 0.43$  eV), with 39 samples and 1.323 Å average; with MAE, the corresponding pattern is defined as ( $\text{EA}_{\text{max}} \leq -0.037$  eV) AND ( $q_{\text{min}} \leq 0.47$  e), with 61 samples and 1.308 Å average. Both patterns significantly exceed the size of the  $l(\text{C-O}) > 1.30$  Å subgroups and contain many samples in common. Among samples not present in both patterns, the pattern obtained with MSE has all adsorption sites on  $\text{La}_2\text{O}_3$ , and the pattern from MAE cost function has sites on  $\text{Na}_2\text{O}$ . Both lanthanum and sodium oxide are materials prone to extremely strong carbonation (Supplementary Table 2). Moreover, the pattern obtained with MAE cost function contains two sites above which  $\text{CO}_2$  prefers to physisorb, with  $l(\text{C-O}) = 1.17$  Å. This clearly demonstrates the tendency of DTR to overemphasize the importance of data points based solely on the value of target property. DTR minimizes the overall cost function, so that the local regularities are not explicitly considered and are smeared out for the sake of optimizing the global fit, whereas the SGD with quality function (2) is exactly focused on revealing such local subsets. As a result, materials with sites where C-O bond is strongly elongated due to a large charge transfer and the sites above which  $\text{CO}_2$  is not activated are selected by DTR together with materials providing moderate charge transfer, but at the same time additional bonding of O atom in adsorbed  $\text{CO}_2$  with a surface cation, which also leads to C-O bond elongation. Thus, DTR in this case fails to distinguish these two very different activation modes and, in some cases, cannot even distinguish activation from non-activation.

### Supplementary notes.

**Studied materials and surface terminations.** In the current study we have focused on semiconductor (or insulating) oxide materials. Furthermore, we do not consider defects (*e.g.*, oxygen vacancies) and charge-carrier doping, which can significantly modify surface chemical properties. Despite these constraints, the selected materials class includes a large number of compounds (binary, ternary, and more complex oxides). Metallic oxides and defects on surfaces will be the object of the next study. In general, three groups of oxides have been considered:  $A^{2+}B^{4+}O_3$ ,  $A^{1+}B^{5+}O_3$ ,  $A^{3+}B^{3+}O_3$  and all the binary oxides  $AO$ ,  $BO_2$ ,  $A_2O_3$ ,  $A_2O$ ,  $B_2O_3$ . For each oxide material we have considered a set of low-index surfaces with maximal Miller index up to 2. We mainly considered non-polar surfaces. For several included polar surfaces, reconstructions that compensate surface charge assuming formal charges of the ions were considered. All surfaces were insulating (with a non-vanishing gap between the highest occupied and lowest unoccupied states). In the cases when oxides have polymorphs ( $TiO_2$ ,  $MgGeO_3$  etc.) they were also included. The full list of materials and surface terminations is shown in Supplementary Table 2. In general, 71 materials have been calculated with 141 surfaces including different terminations. Considering all non-equivalent adsorption sites on these surfaces, the total number of calculated unique  $CO_2$  adsorption geometries is 255. All data, including initial and final geometries, and the computed properties, are available in the NOMAD database<sup>16</sup>.

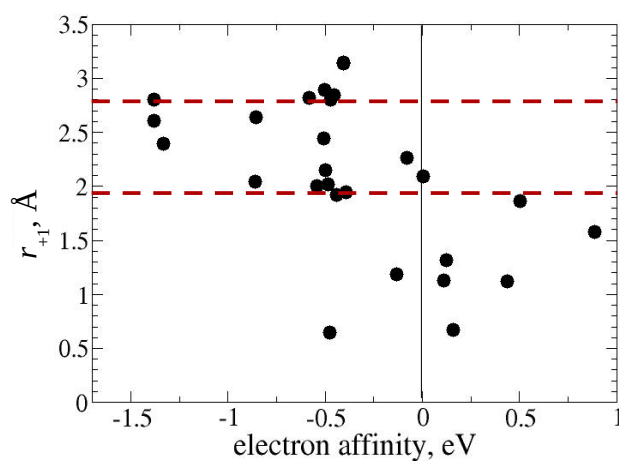
**Supplementary Table 2.** Oxide materials, surface terminations, and the number of unique adsorption sites per termination.

material	surfaces	number of unique sites per surface
MgSiO <sub>3</sub>	(001) MgO-term.	1
MgTiO <sub>3</sub>	(001) (012)	1 2
MgGeO <sub>3</sub> hexagon.	(001) (012)	1 2
MgGeO <sub>3</sub> tetragon.	(001) MgO-term. (001) GeO <sub>2</sub> -term.	1 1
MgSnO <sub>3</sub>	(100)	2
CaSiO <sub>3</sub>	(001) CaO-term. (001) SiO <sub>2</sub> -term. (110) CaO-term. (110) SiO <sub>2</sub> -term.	1 1 1 1
CaTiO <sub>3</sub>	(010) CaO-term. (101) CaO-term. (100) TiO <sub>2</sub> -term.	1 1 1
CaGeO <sub>3</sub>	(001) CaO-term. (001) GeO <sub>2</sub> -term. (110) CaO-term.	1 2 1

	(110) GeO <sub>2</sub> -term.	2
CaZrO <sub>3</sub>	(010) CaO-term.	1
	(101) CaO-term.	2
	(101) ZrO <sub>2</sub> -term.	1
CaSnO <sub>3</sub>	(001) SnO <sub>2</sub> -term.	1
	(110) CaO-term.	2
	(110) SnO <sub>2</sub> -term.	1
SrSiO <sub>3</sub>	(001) SrO-term.	1
SrTiO <sub>3</sub>	(001) SrO-term.	1
	(001) TiO <sub>2</sub> -term.	1
SrGeO <sub>3</sub>	(100) SrO-term.	1
	(100) TiO <sub>2</sub> -term.	1
SrZrO <sub>3</sub>	(001) ZrO <sub>2</sub> -term.	1
	(110) SrO-term.	2
SrSnO <sub>3</sub>	(001) SrO-term.	1
	(001) SnO <sub>2</sub> -term.	1
	(110) SrO-term.	1
	(110) SnO <sub>2</sub> -term.	1
BaSiO <sub>3</sub>	(100)	2
	(101)	1
BaTiO <sub>3</sub>	(001) BaO-term.	1
	(001) TiO <sub>2</sub> -term.	1
BaGeO <sub>3</sub>	(001) BaO-term.	1
BaZrO <sub>3</sub>	(001) ZrO <sub>2</sub> -term.	1
	(110) BaO-term.	1
BaSnO <sub>3</sub>	(001) BaO-term.	1
	(001) SnO <sub>2</sub> -term.	1
MgO	(001)	1
	(110)	1
	(111) octopolar O-term.	1
CaO	(001)	1
	(110)	1
	(111) octopolar O-term.	1
SrO	(001)	1
	(110)	1
	(111) octopolar O-term.	1
BaO	(001)	1
	(110)	1
	(111) octopolar O-term.	1
SiO <sub>2</sub>	(001)	2
TiO <sub>2</sub> anatase	(101)	2
	(001)	1
TiO <sub>2</sub> rutile	(100)	1
	(110)	2
GeO <sub>2</sub>	(100)	1
	(110)	2
ZrO <sub>2</sub>	(001)	2
	(011)	4
	(111)	3
SnO <sub>2</sub>	(100)	1
	(110)	2

ZnO	(10-10)	1
LiNbO <sub>3</sub>	(100)	1
NaNbO <sub>3</sub> tetragon.	(010) (110)	2 1
NaNbO <sub>3</sub> P bcm	(100)	1
KNbO <sub>3</sub> tetragon.	(010) (110)	1 2
RbNbO <sub>3</sub> P1	(111)	2
CsNbO <sub>3</sub>	(010) (100)	2 1
LiVO <sub>3</sub> orthogon.	(110)	2
LiVO <sub>3</sub> P bcm	(100)	1
NaVO <sub>3</sub>	(010) (110)	1 1
KVO <sub>3</sub> orthogon.	(010)	1
RbVO <sub>3</sub> tetragon.	(010) (110)	1 1
RbVO <sub>3</sub> P bcm	(100)	1
CsVO <sub>3</sub> tetragon.	(010) (110)	1 1
LiSbO <sub>3</sub> tetragon.	(010)	1
LiSbO <sub>3</sub> P bcm	(100)	1
NaSbO <sub>3</sub> tetragon.	(010)	1
NaSbO <sub>3</sub> P bcm	(100)	2
KSbO <sub>3</sub> tetragon.	(110)	2
Na <sub>2</sub> O	(011) (111)	1 1
GaAlO <sub>3</sub>	(100)	2
InAlO <sub>3</sub> hexagon.	(110)	2
InAlO <sub>3</sub> orthorh.	(010) (110) (121)	3 4 3
GaInO <sub>3</sub>	(100) (110) (120)	2 5 6
ScAlO <sub>3</sub>	(010) (100) (110) (121)	1 2 2 6
ScGaO <sub>3</sub>	(010) (110)	3 5
ScInO <sub>3</sub>	(100) (110) In <sub>2</sub> O <sub>3</sub> -term. (110) ScInO <sub>3</sub> -term. (121)	5 5 5 6
YScO <sub>3</sub>	(100)	1
LaScO <sub>3</sub>	(100)	1
YInO <sub>3</sub>	(100)	2

	(110)	2
YAlO <sub>3</sub>	(011) (100)	2 1
LaYO <sub>3</sub>	(001)	2
YGaO <sub>3</sub>	(100) (110)	2 2
LaAlO <sub>3</sub>	(110)	2
LaGaO <sub>3</sub>	(100) (110)	1 1
LaInO <sub>3</sub>	(100)	1
Al <sub>2</sub> O <sub>3</sub>	(001) (012)	1 1
Ga <sub>2</sub> O <sub>3</sub>	(110) (212)	3 7
Sc <sub>2</sub> O <sub>3</sub>	(001) (110) (111)	3 5 5
In <sub>2</sub> O <sub>3</sub>	(001) (110) (111)	1 5 4
La <sub>2</sub> O <sub>3</sub>	(100) (110) (120) (201)	2 2 3 2



**Supplementary Figure 4.** The dependence of LUMO radii ( $r_{+1}$ ) on electron affinities. Red dashed lines show isovalues  $r_{+1} = 1.94 \text{ \AA}$  and  $2.80 \text{ \AA}$ .

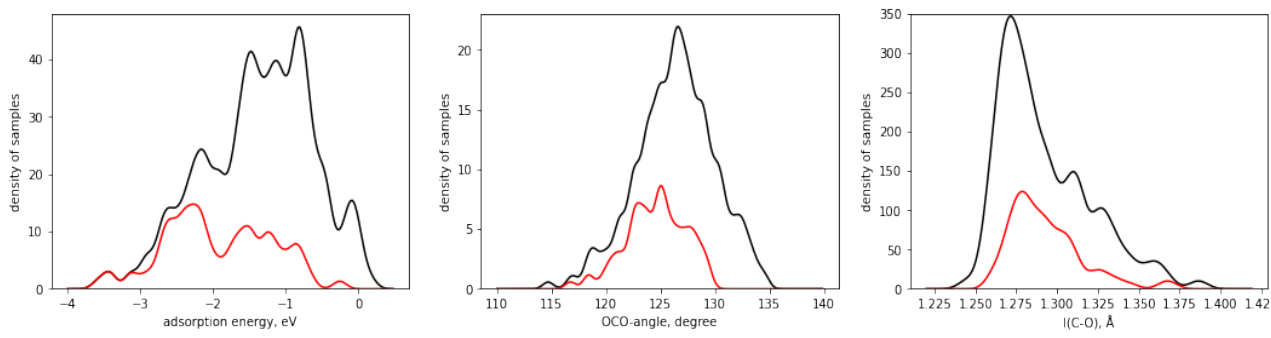
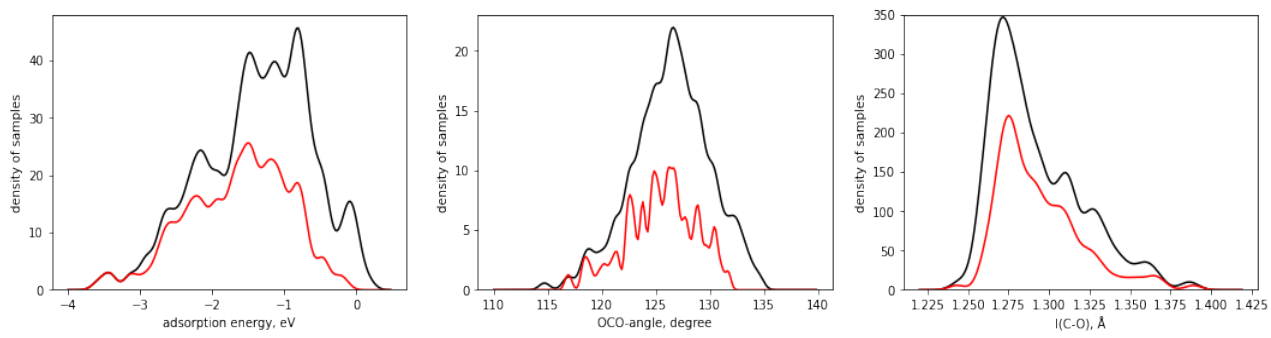
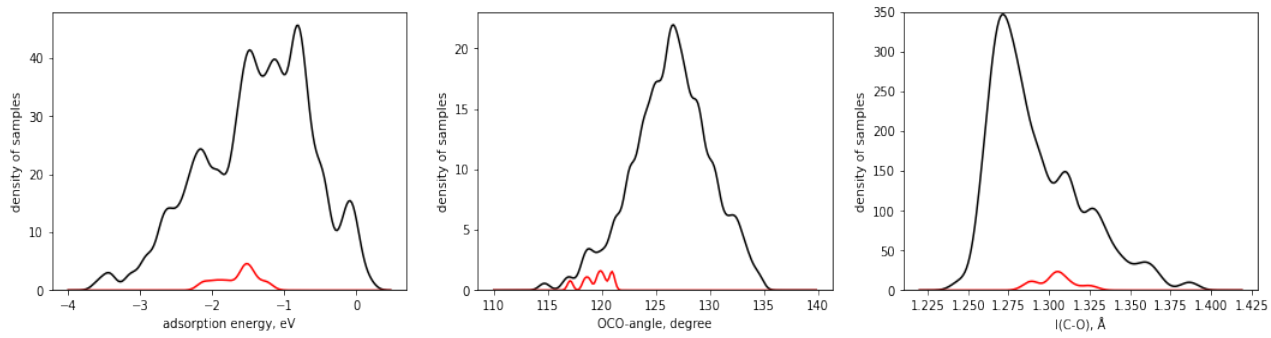
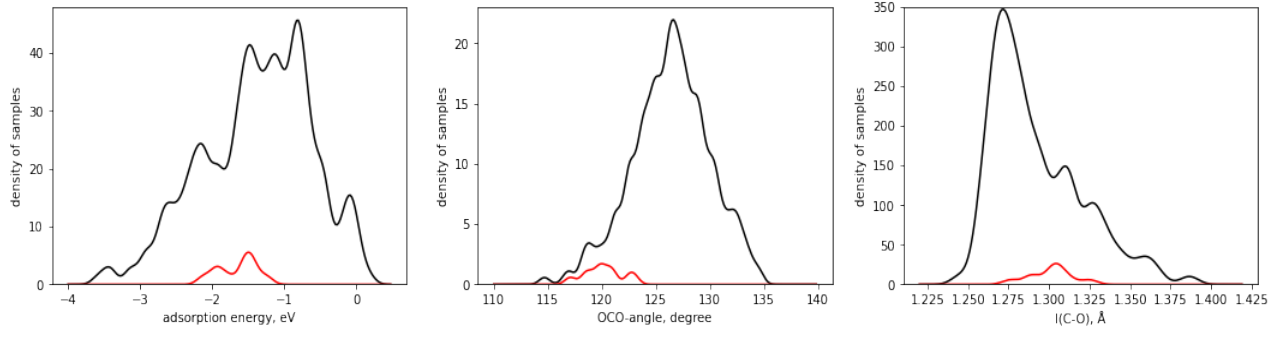
**Supplementary Table 3.** The full list of used primary features calculated with PBEsol.

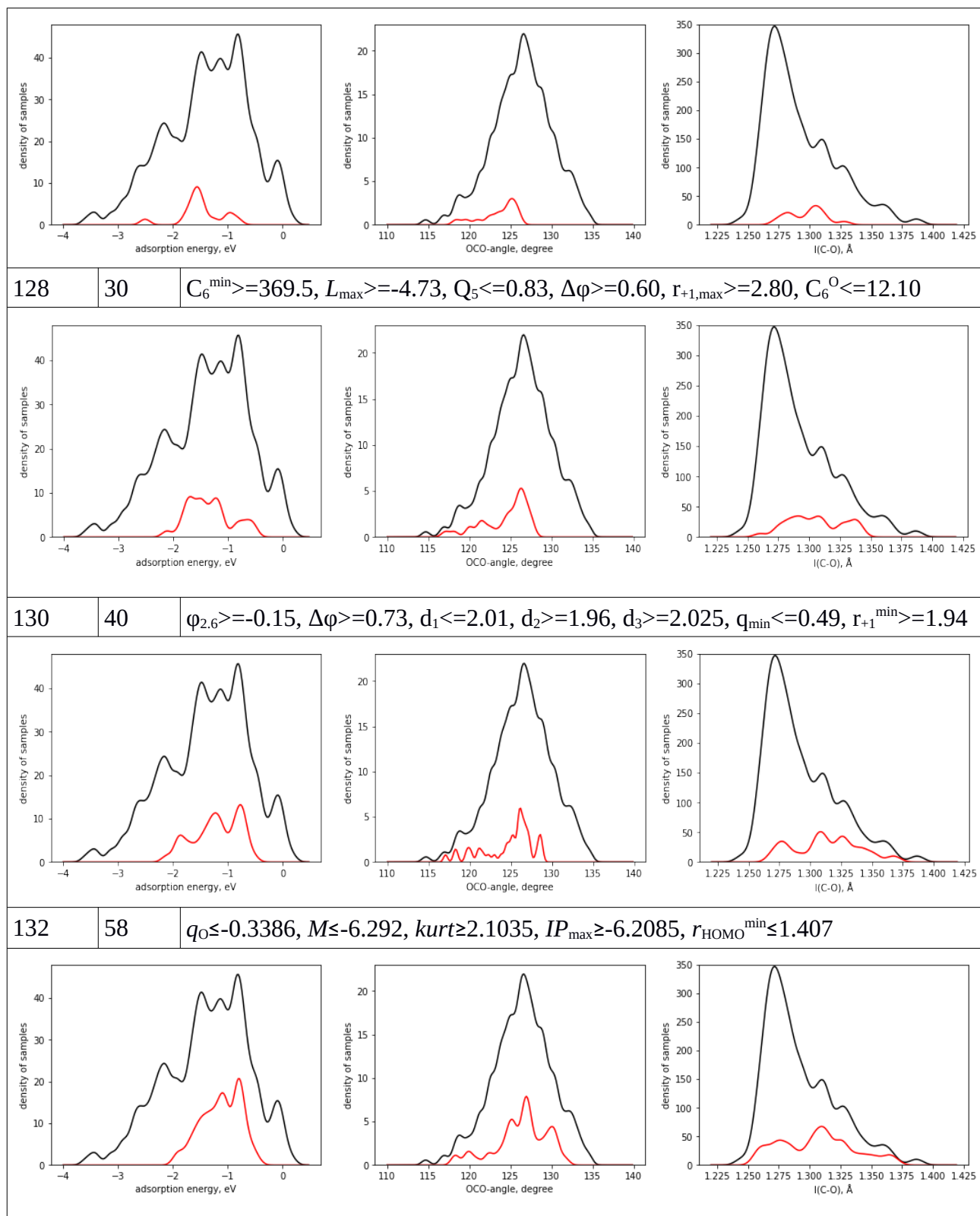
symbol	meaning
$IP_{\min/\max}, IP_O$	ionization potential, minimal and maximal in the pair of atoms $A$ and $B$ , and for $O$ ; calculated as $E_{\text{atom}} - E_{\text{cation}}$

$EA_{\min/\max}$ , $EA_{\text{O}}$	electron affinity, minimal and maximal in the pair of atoms $A$ and $B$ , and for O; calculated as $E_{\text{anion}} - E_{\text{atom}}$
$EN_{\min/\max}$ , $EN_{\text{O}}$	Mulliken electronegativity, minimal and maximal in the pair of atoms $A$ and $B$ , and for O
$r_{\text{HOMO}}, r_{+1}, r_{-1}$	maximum value of radial wave functions of the non-spin polarized spherically symmetric atom for HOMO, LUMO and HOMO-1
$\Delta$	band gap of the whole surface slab
$E_{\text{form}}$	surface formation energy
$VBM$	valence-band maximum with respect to vacuum level
$W$	work function ( $W = -VBM$ )
$q_{\text{O}}$	Hirshfeld charge of O-atom
$q_{\min}, q_{\max}$	minimal and maximal Hirshfeld charges of cations in the pair $A$ and $B$ , calculated as an average for all surface cations of a given type
$\varphi_{1.4}, \varphi_{2.6}, \varphi_{1.4} - \varphi_{2.6}$	electrostatic potentials above O-atom at 1.4 and 2.6 Å and their difference. 1.4 Å corresponds to the average length of the bond between C and surface O, 2.6 Å is the minimal distance from surface O to C-atom of physisorbed carbon-dioxide molecule as observed from our calculations
$\alpha_{\text{O}}, C_6^{\text{O}}$	polarizability and $C_6$ -coefficient for O-atom obtained from many-body dispersion scheme [16]
$\alpha_{\min}, \alpha_{\max}, C_6^{\min}, C_6^{\max}$	polarizability and $C_6$ -coefficient for cations, minimal and maximal in the pair $A$ and $B$ , calculated as an average for all surface cations of a given type
$Q_5, Q_6$	local-order parameter with $l = 5$ or $6$
$d_1, d_2, d_3$	distances from surface O-atom to the first-, second-, and third-nearest cations
$BV$	bond-valence value of O-atom
$PC$	weighted O $2p$ -band center
$C_{\min}, C_{\max}$	first moment for PDOS of cation within valence-band, minimal and maximal in the pair $A$ and $B$ , calculated as an average for all surface cations of a given type
$wid$	square-root of the second moment of O $2p$ -band
$wid_{\min}, wid_{\max}$	square-root of the second moment for PDOS of cations within valence-band, minimal and maximal in the pair $A$ and $B$ , calculated as an average for all surface cations of a given type
$skew$	skewness of O $2p$ -band PDOS
$kurt$	kurtosis of O $2p$ -band PDOS
$CBm$	conduction band minimum
$L_{\min}, L_{\max}$	energy of lowest unoccupied state of cation, minimal and maximal in the pair $A$ and $B$ , calculated as an average for all surface cations of a given type
$M$	energy at which the O $2p$ -band PDOS is maximal
$U$	eigenstate with least negative value in O $2p$ -band

**Supplementary Table 4.** Top subgroups obtained by minimization of OCO-angle with/without energy constraint and corresponding distributions of samples according to adsorption energies, OCO-angles, and C-O bond distances.

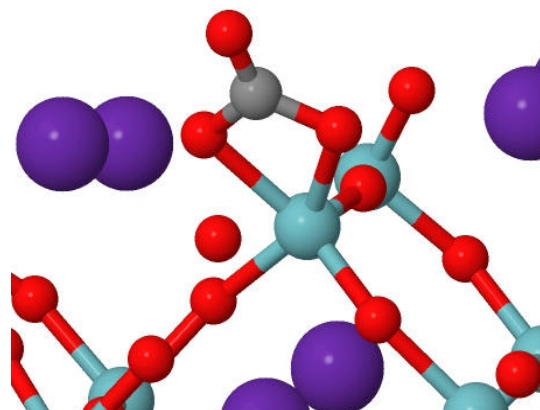
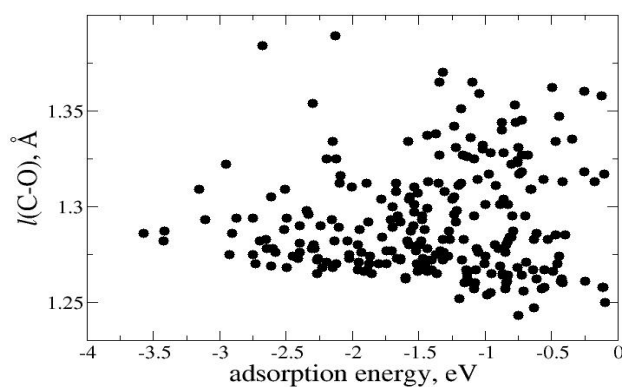
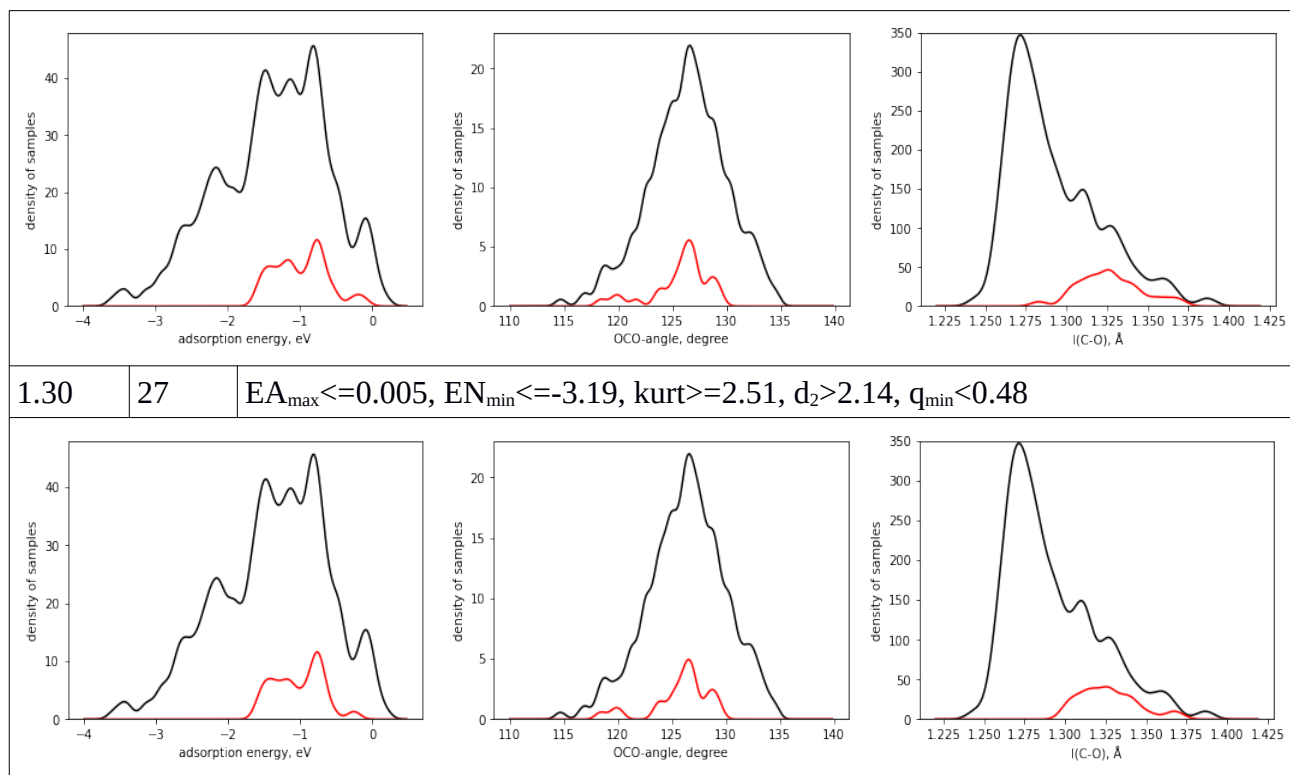
cutoff	size	selector
without adsorption energy constraint		
123	9	$q_0 > -0.39$ , $Q_5 \leq 0.81$ , $\Delta > 1.675$ , $PC > -6.61$ , $q_{\min} \leq 0.58$
124	14	$L_{\min} > -1.76$ , $Q_5 > 0.69$ , $\alpha_{\max} > 100.4$ , $c_{\max} \leq -6.00$ , $\alpha_O \leq 1.63$
126	19	$L_{\max} > -2.70$ , $IP_{\max} \geq -6.05$ , $\alpha_{\max} \leq 184.5$ , $\Delta\phi > 1.33$ , $q_{\max} \leq 0.59$ , $wid \leq 1.59$ , $wid \geq 0.58$
128	44	$EA_{\max} \geq -0.425$ , $Q_6 > 0.51$ , $\alpha_{\max} \geq 50.4$ , $\Delta\phi > 1.00$ , $q_{\min} \leq 0.49$

130	77	$L_{\max} \geq -5.23$ , $EA_{\max} \leq 0.16$ , $d_1 \geq 1.82$ , $d_2 > 2.10$
		
132	139	$IP_{\max} \geq -6.99$ , $q_0 \leq -0.32$ , $C_6^O \geq 10.36$
		
with adsorption energy constraint		
123	8	$Q_6 < 0.66$ , $c_{\max} \geq -9.80$ , $d_2 \geq 2.00$ , $M \leq -4.12$ , $wid_{\min} > 1.52$
		
124	10	$q_0 \leq -0.32$ , $Q_6 < 0.66$ , $Q_6 \geq 0.57$ , $\Delta\phi = 0.60$ , $r_{-1}^{\max} \leq 1.65$ , $wid \geq 1.24$
		
126	15	$L_{\min} \geq -5.1085$ , $\varphi_{2.6} \leq 0.3033$ , $\Delta\phi \leq 1.0622$ , $d_1 \geq 1.82$ , $d_2 \geq 2.005$ , $r_{+1}^{\max} > 2.83$



**Supplementary Table 5.** Top subgroups obtained by maximization of  $l(\text{C-O})$ -bond with/without energy constraint and corresponding distributions of samples according to adsorption energies, OCO-angles, and C-O bond distances.

cutoff	size	selector
without adsorption energy constraint		
1.26	121	$C_6^{\min} \geq 343.5$ , $\phi_{2.6} \leq 0.66$ , $Q_5 \leq 0.83$ , $M \geq -8.05$
1.28	38	$EA_{\max} \leq 0.005$ , $d_2 > 2.22$ , $M \leq -4.12$
1.30	27	$kurt \geq 2.10$ , $d_2 > 2.14$ , $U \leq -5.34$ , $q_{\min} < 0.48$
with adsorption energy constraint		
1.26	56	$CBM \geq -5.17$ , $\Delta\phi \leq 1.13$ , $PC \geq -8.62$ , $d_3 \leq 2.48$ , $M \leq -6.06$
1.28	30	$W \geq 5.1$ , $d_2 > 2.14$ , $q_{\min} < 0.48$



**Supplementary Figure 5.** (left) The dependence of CO<sub>2</sub> adsorption energy on C-O bond length  $l(\text{C-O})$ . (right) Typical CO<sub>2</sub> adsorption structure from the subgroup with larger  $l(\text{C-O})$ . Color scheme: gray C, red O, cyan Nb, violet Rb.

### Supplementary discussion.

**1. Dipole moment of the slab induced by adsorbed CO<sub>2</sub> molecule.** The dipole moment of the slab with adsorbed CO<sub>2</sub> molecule indicates both the bending of the molecule and the amount of charge transferred to the molecule upon adsorption (the dipole moment of the slab before adsorption is zero, since we use symmetrically terminated slabs), and thus it indicates the molecule activation. Since in our models the CO<sub>2</sub> adsorption was considered on one side of a surface slab, the dipole

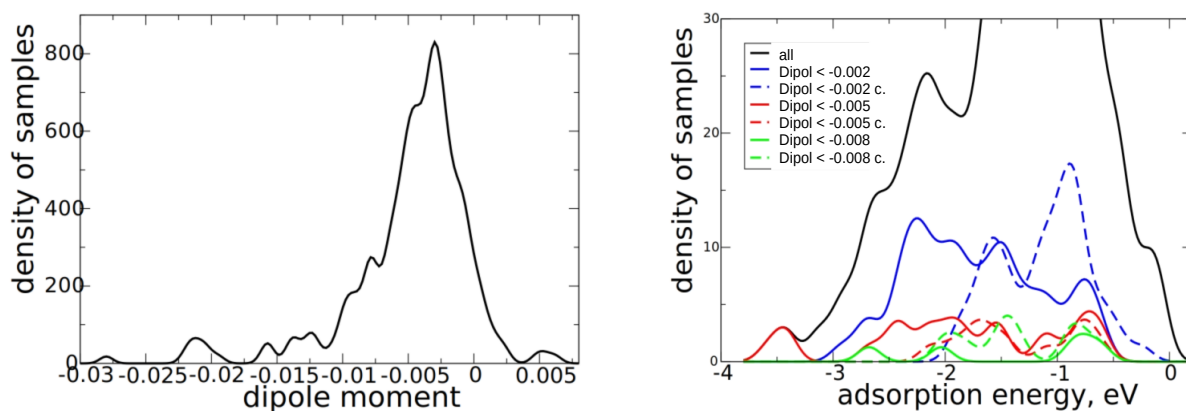
moment can be calculated as the difference of electrostatic potentials in vacuum at the two sides of the slab normalized per the surface area. The distribution of the calculated dipole moments in our data shows that certain number of samples has a positive dipole moment (Supplementary Figure 6, left), which is the result of surface relaxation upon CO<sub>2</sub> adsorption. We have performed SGD with the minimization of the dipole moment (eq. 1 of the main text), which corresponds to a larger amount of electron density transferred to the CO<sub>2</sub> molecule. Three thresholds have been chosen – -0.002, -0.005, and -0.008. For the cases with both Sabatier principle constrain and without it obtained subgroups are shown in Supplementary Table 6.

The distribution of adsorption energies for obtained subgroups is shown in Supplementary Figure 6 left. In all cases where no Sabatier principle constraint was introduced in the quality function there are samples for which strong carbonation is observed with adsorption energies around -3 eV.

Among subgroups obtained with Sabatier principle constraint the one with -0.002 threshold is mostly populated (Supplementary Table 6). It contains adsorption sites on several mentioned in the main text good catalysts – LaAlO<sub>3</sub>, Ga<sub>2</sub>O<sub>3</sub>, but also on a less promising YInO<sub>3</sub>. Regarding other materials from this subgroup there is no reliable information.

**Supplementary Table 6.** The subgroups obtained for SGD minimization of a dipole moment.

threshold	size	subgroup
Dipole minimization without Sabatier principle constraint		
-0.002	57	$d_1 \leq 2.2025, d_3 \leq 2.9045, U \geq -6.108, r_{+1}^{\max} \leq 2.8315$
-0.005	23	$L_{\min} > -2.19, EA_{\max} \geq -0.464, Q_5 \leq 0.8113, Q_6 \leq 0.7756, r_{-1}^{\max} \leq 1.652$
-0.008	5	$L_{\min} > -2.538, EA_{\max} \leq 0.157, d_1 < 1.8635, d_2 < 2.037, r_{+1}^{\min} \leq 2.093$
Dipole minimization with Sabatier principle constraint		
-0.002	46	$CBM \geq -5.1675, q_0 \geq -0.3906, Q_5 \geq 0.51525, VBM \leq -5.7975, M \geq -7.285, q_{\max} \leq 0.64775, r_{\text{HOMO}}^{\min} \geq 0.581$
-0.005	12	$L_{\min} > -2.19, EN_{\min} \leq -3.275, r_{+1}^{\min} \leq 2.807, wid \geq 1.242$
-0.008	8	$\varphi_{2.6} \leq 0.66395, IP_{\min} \leq -5.831, c_{\min} > -9.361, kurt \leq 8.576, q_{\min} < 0.43575$



**Supplementary Figure 6.** (left) The distribution of samples according to the calculated dipole moment in the whole data set. (right) The distribution of adsorption energies in obtained subgroups.

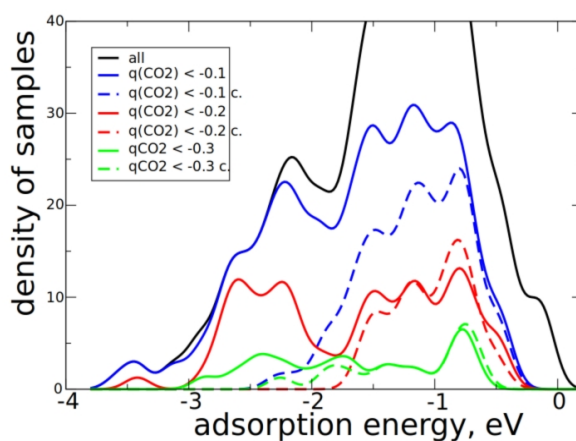
**2. Hirshfeld charge of an adsorbed CO<sub>2</sub>.** The physical reasoning behind this indicator is the same as in the case of the dipole moment. Although partitioning of electron density among atoms in a solid is not uniquely defined, different partitioning schemes and in particular Hirshfeld partitioning<sup>18</sup> qualitatively capture changes in electron distribution. SGD was performed with quality function shown in eq. 1 of the main text. Three thresholds were considered – -0.1, -0.2 and -0.3 *e*. Obtained SGD subgroups are shown in Supplementary Table 6.

The distribution of adsorption energies for corresponding subgroups is presented in Supplementary Figure 7. For the unconstrained case there is again a domain of samples with large absolute values of adsorption energies. All subgroups obtained with and without Sabatier principle constraint overlap significantly with reduced OCO subgroups. For example the overlap between unconstrained OCO < 132° and  $q(\text{CO}_2) < 0.1 e$  subgroups is 91% and 74% of the population respectively, and for corresponding Sabatier principle constrained subgroups – 69 % and 49%.

**Supplementary Table 6.** The subgroups obtained for SGD minimization of adsorbed CO<sub>2</sub> Hirshfeld charge –  $q(\text{CO}_2)$ .

threshold	size	subgroup
<i>q</i> (CO <sub>2</sub> ) minimization without Sabatier principle constraint		
-0.1	171	$q_{\text{O}} \leq -0.3386, Q_6 \leq 0.9458, \Delta \leq 4.07$
-0.2	72	$\varphi_{1.4} \geq 1.051, Q_5 \leq 0.82885, E_{\text{form}} < 0.077$
-0.3	22	$IP_{\text{min}} < -6.4695, IP_{\text{max}} \geq -5.941, q_{\text{O}} < -0.371, d_2 \geq 2.037, r_{+1}^{\text{min}} \leq 2.093$
<i>q</i> (CO <sub>2</sub> ) minimization with Sabatier principle constraint		
-0.1	82	$IP_{\text{max}} \geq -5.941, VBM \leq -5.0995, \Delta \varphi \geq 0.7326, r_{-1}^{\text{min}} \leq 1.652, \alpha_{\text{O}} \leq 3.11045$
-0.2	39	$EA_{\text{max}} \leq 0.005, EA_{\text{max}} \geq -0.4945, \Delta \varphi \geq 0.7326, r_{-1}^{\text{min}} \leq 1.666, E_{\text{form}} \leq 0.085$

-0.3	15	$C_6^{\min} > 485.0$ , $c_{\min} \leq -9.58$ , $kurt \geq 3.1545$ , $E_{\text{form}} < 0.062$
------	----	---



**Supplementary Figure 7.** The distribution of adsorption energies in the subgroups of samples with larger absolute values of Hirshfeld charge of an adsorbed  $\text{CO}_2$ .

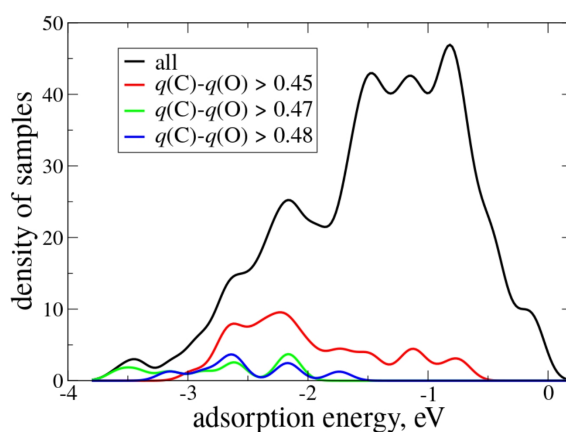
**3. Difference in Hirshfeld charges of C and O atoms in an adsorbed  $\text{CO}_2$ .** This property indicates the ionicity of a C-O bond. Larger ionicity is expected to correlate with the reactivity in reactions with electrophilic or nucleophilic agents. The calculated  $\text{CO}_2$  gas-phase value of the charge difference is  $0.44 e$ . It lies within the range of the data for adsorbed  $\text{CO}_2$ , namely,  $0.38$ - $0.52 e$  (Supplementary Figure 8, left). We have done the SGD search of subgroups with positive shift with three cutoffs:  $0.45$ ,  $0.47$ , and  $0.48 e$ . Obtained subgroups are shown in Supplementary Table 7.

In the case when no Sabatier principle constraint was accounted for, all subgroups contain the samples for which strong carbonation is observed (Supplementary Figure 8). There is a certain overlap with reduced OCO subgroups. For example, the subgroup  $q(\text{C})-q(\text{O}) > 0.45e$  contains 18 common samples (49%) with  $\text{OCO} < 130^\circ$  subgroups. The subgroups obtained with Sabatier principle constraint also partially overlap with constrained OCO subgroups – 10 common samples for  $q(\text{C})-q(\text{O}) > 0.45e$  with  $\text{OCO} > 128^\circ$  and 16 with  $\text{OCO} > 130^\circ$  subgroups. Even larger relative overlap is obtained with  $l(\text{C-O}) > 1.30 \text{ \AA}$  subgroup – 16 samples (67%). Smaller size constrained subgroups with  $0.47$  and  $0.48e$  cutoffs have also about 60% common samples with  $l(\text{C-O}) > 1.30 \text{ \AA}$  subgroup.

**Supplementary Table 7.** The subgroups obtained for SGD maximization of the difference in Hirshfeld charges of C and O atoms.

threshold	size	subgroup
$q(\text{CO}_2)$ minimization without Sabatier principle constraint		
0.45	37	$W < 5.5255$ , $PC > -7.53$ , $C_6 \leq 11.1305$ , $\text{skew} > = -2.1615$

0.47	9	$L_{\max} > -1.2615$ , $\varphi_{1.4} > 1.2116$ , $\alpha_{\text{O}} < -0.1558$
0.48	8	$\Delta\varphi > 0.996$ , $M > -5.1865$ , $q_{\max} > 0.5483$
$q(\text{CO}_2)$ minimization with Sabatier principle constraint		
0.45	24	$EN_{\min} \leq 3.633$ , $EN_{\max} > -3.039$ , $PC > -8.895$ , $r_{\text{HOMO}}^{\min} \leq 1.337$
0.47	7	$C_6^{\max} > 1440.5$ , $C_6^{\min} \leq 830.5$ , $Q_5 \leq 0.7952$ , $d_2 > 2.217$ , $r_{\text{HOMO}}^{\max} \geq 1.344$
0.48	7	$C_6^{\max} > 1440.5$ , $C_6^{\min} \leq 830.5$ , $Q_5 \leq 0.7952$ , $d_2 > 2.217$ , $r_{\text{HOMO}}^{\max} \geq 1.344$



**Supplementary Figure 8.** The distribution of adsorption energies in the subgroups with increased  $q(\text{C})-q(\text{O})$  without Sabatier principle constraint.

**4. Difference of Hirshfeld charges on O-atoms of an adsorbed  $\text{CO}_2$ .** As we show, the elongated C-O bonds are observed when the  $\text{CO}_2$  molecule is adsorbed in an asymmetric position, so that one oxygen atom is bonded with a surface cation and the other one is protruding. In these cases, the two O-atoms have nonequivalent chemical surroundings. Correspondingly, the difference of Hirshfeld charges on  $\text{CO}_2$  oxygens,  $\Delta q(\text{O})$ , is expected to indicate this asymmetry. The SGD with the absolute  $\Delta q(\text{O})$  as target property was performed with maximizing this difference with the quality function (1) in the main text. The next thresholds have been considered: 0.01, 0.02 and 0.03  $e$ . Obtained subgroups are summarized in Supplementary Supplementary Table 8.

The analysis of their populations shows significant overlap with the subgroups for elongated C-O bond distances. For instance, there are 21 common samples in  $l(\text{C}-\text{O}) > 1.3 \text{ \AA}$  subgroup and the subgroup with  $\Delta q(\text{O}) > 0.01 e$ , 81% and 78% of respective populations. The overlap for constrained and unconstrained with Sabatier principle subgroups is 100%. The samples in  $\Delta q(\text{O})$  subgroups with larger thresholds are mostly the same as ones in  $\Delta q(\text{O}) > 0.01 e$  subgroup. So, we conclude that the difference of Hirshfeld charges on  $\text{CO}_2$  oxygen atoms basically reproduces the C-O bond length indicator.

**Supplementary Table 8.** The subgroups obtained for SGD maximization of Hirshfeld charges difference on O-atoms in an adsorbed CO<sub>2</sub>.

threshold	size	subgroup
maximization of $\Delta q(\text{O})$ without Sabatier principle constraint		
0.01	25	$\Delta\phi \geq 0.596$ , $PC \leq -7.207$ , $d_2 > 2.217$ , $r_1^{\min} \leq 1.1235$
maximization of $\Delta q(\text{O})$ with Sabatier principle constraint		
0.01	26	$EA_{\max} \leq 0.005$ , $c_{\min} \leq -5.849$ , $d_2 > 2.217$ , $q_{\min} \leq 0.51$
0.02	19	$C_6^{\max} \geq 580.5$ , $EA_{\max} \leq 0.0375$ , $\phi_{1.4} \geq 0.66415$ , $IP_{\min} \leq 6.4695$ , $\alpha_{\max} > 90.75$ , $C_6 \geq 9.025$
0.03	11	$IP_{\max} > -5.5225$ , $\alpha_{\min} \leq 60.55$ , $d_1 \leq 1.9585$ , $M \geq -7.555$ , $\alpha_0 \geq 0.2268$

### Supplementary References

- Blum, V. et al. Ab initio molecular simulations with numeric atom-centered orbitals. *Comput. Phys. Comm.* **180**, 2175-2196 (2009).
- Perdew, J. P., Burke, K. & Ernzerhof, M. Generalized gradient approximation made simple. *Phys. Rev. Lett.* **77**, 3865–3868 (1997).
- Perdew, J. P. et al. Restoring the density-gradient expansion for exchange in solids and surfaces. *Phys. Rev. Lett.* **100**, 136406 (2008).
- Tkatchenko, A. & Scheffler, M. Accurate molecular van der Waals interactions from ground-state electron density and free-atom reference data. *Phys. Rev. Lett.* **102**, 073005 (2009).
- Ceperley, D. M. & Alder, B. J. Ground state of the electron gas by a stochastic method. *Phys. Rev. Lett.* **45**, 566–569 (1980).
- Hammer, B., Hansen, L. B. & Nørskov, J. K. Improved adsorption energetics within density-functional theory using revised Perdew-Burke-Ernzerhof functionals. *Phys. Rev. B* **59**, 7413-7421 (1999).
- Blaylock, D. W., Ogura, T., Green, W. H. & Beran, G. J. O. Computational investigation of thermochemistry and kinetics of steam methane reforming on Ni(111) under realistic conditions. *J. Phys. Chem. C* **113**, 4898-4908 (2009).
- Peterson, A. A., Abild-Pedersen, F., Studt, F., Rossmeisl & J., Nørskov, J. K. How copper catalyzes the electroreduction of carbon dioxide into hydrocarbon fuels. *Energy Environ. Sci.* **3**, 1311-1315 (2010).
- Neugebauer, J. & Scheffler, M. Adsorbate-substrate and adsorbate-adsorbate interactions of Na and K adlayers on Al(111). *Phys. Rev. B* **46**, 16067-16080 (1992).
- Solis, B. H. et al. Initial stages of CO<sub>2</sub> adsorption on CaO: a combined experimental and computational study. *Phys. Chem. Chem. Phys.* **19**, 4231-4242 (2017).
- Wang, Y. et al. CO<sub>2</sub> activation by ZnO through the formation of an unusual tridentate surface carbonate. *Angew. Chem. Int. Ed.* **46**, 5624–5627 (2007).
- Xia, X., Strunk, J., Busser, W., Naumann d’Alnoncourt, R. & Muhler, M. Probing the surface heterogeneity of polycrystalline zinc oxide by static adsorption microcalorimetry. 1. The influence of the thermal pretreatment on the adsorption of carbon dioxide. *J. Phys. Chem. C* **112**, 10938–10942 (2008).
- Bučko, T., Lebegue, S., Angyan, J. G. & Hafner, J. Extending the applicability of the Tkatchenko-Scheffler dispersion correction via iterative Hirshfeld partitioning. *J. Chem. Phys.* **141**, 034114 (2014).
- Meixner, D., Arthur, D. & George, S. Kinetics of desorption, adsorption, and surface diffusion of CO<sub>2</sub> on MgO(100). *Surf. Sci.* **261**, 141–154 (1992).

15. Mazheika, A. & Levchenko, S. V. Ni Substitutional Defects in bulk and at the (001) surface of MgO from first-principles calculations. *J. Phys. Chem. C* **120**, 26934–26944 (2016).
16. <http://nomad-repository.eu/>
17. Hinuma, Y., Hayashi, H., Kumagai, Y., Tanaka, I. & Oba, F. *Phys. Rev. B* **96**, 094102 (2017).
18. Hirshfeld, F. L. Bonded-atom fragments for describing molecular charge densities. *Theor. Chim. Acta*, **44**, 129–138 (1977).